De-Gaussification by Inconclusive Photon Subtraction

S. Olivares* and M. G. A. Paris**

Dipartimento di Fisica, Università degli Studi di Milano, Italy
*e-mail: Stefano.Olivares@mi.infn.it;
**e-mail: Matteo.Paris@fisica.unimi.it
Received May 6, 2006

Abstract—We address conditional de-Gaussification of continuous variable states by inconclusive photon subtraction (IPS) and review in detail its application to the bipartite twin-beam state of radiation. The IPS map in the Fock basis and counterpart in the phase space have been derived. Teleportation assisted by IPS states is analyzed, and the corresponding fidelity is evaluated as a function of the involved parameters. Nonlocality of IPS states is investigated by means of different tests, including displaced parity, homodyne detection, pseudospin, and displaced on/off photodetection. Dissipation and thermal noise and nonunit quantum efficiency are taken into account in the detection stage. We show that the IPS process, for a suitable choice of the involved parameters, improves teleportation fidelity and enhances nonlocal properties.

1. INTRODUCTION

Nonclassical properties of a radiation field play a relevant role in modern information processing, since, in general, they improve continuous variable (CV) communication protocols based on light manipulation [1, 2]. Indeed, quantum light finds application in several fundamental tests of quantum mechanics [3], as well as in high-precision measurements and high-capacity communication channels [4, 5]. Among nonclassical features, entanglement plays a major role, being the essential resource for quantum computing, teleportation, and cryptographic protocols. Recently, CV entanglement has also proven to be a valuable tool for improving optical resolution, spectroscopy, interferometry, tomography, and discrimination of quantum operations. Recent experimental realizations also include dense coding [6] and a teleportation network [7].

Entanglement in optical systems is usually generated through parametric downconversion in nonlinear crystals. The resulting bipartite state, the so-called twin-beam state of radiation (TWB), allows the realization of several beautiful experiments and the demonstration of the above quantum protocols. However, the resources available to generate CV entangled states are unavoidably limited: nonlinearities are generally small, and, in turn, the resulting states have a limited amount of entanglement and energy. In this context, practical applications require novel schemes to create more entangled states or to increase the degree of entanglement of a given signal.

In quantum mechanics, the reduction postulate provides an alternative mechanism to achieve *effective* nonlinear dynamics. In fact, if a measurement is performed on a portion of a composite system, the output state strongly depends on the results of the measurement. As a consequence, the *conditional* state of the unmeasured part, i.e., the subensemble corresponding to a given outcome, may be connected to the initial one by a (strongly) nonlinear map. In this paper, we focus our attention on a scheme of this kind and address a conditional method based on subtraction of photons to enhance nonclassical features. In particular, we analyze how, and to what extent, photon subtraction may be used to increase nonlocal correlations of twin beams. As we will see, photon subtraction transforms the Gaussian Wigner function of TWB into non-Gaussian one, and therefore it is also referred to as a *de-Gaussification* process.

The photon subtraction process on TWBs was first proposed in [8], where a well-defined number of photons is subtracted from both parties of a TWB by transmitting each mode through a beam splitter and performing a joint photon-number measurement on the reflected beams. The degree of entanglement is then increased, and the fidelity of the CV teleportation assisted by a such photon-subtracted state is improved [9]. However, this scheme is based on the possibility of resolving the actual number of revealed photons. In [10] we showed that the improvement of teleportation fidelity is possible also when the number of detected photon is not known. In our scheme, we use on/off avalanche photodetectors able only to distinguish the presence from the absence of radiation. For this reason, we referred to this method as inconclusive photon subtraction (IPS). The single-mode version of this process has been recently implemented [11], and the nonclassicality of the generated state starting from squeezed vacuum has been theoretically investigated [12, 13]. In addition, nonlocal properties of the photon-subtracted TWBs have been investigated by means of different nonlocality tests [14–19], finding enhanced nonlocal
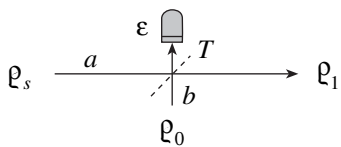
Fig. 1. Scheme of the IPS process: the input state ϱ_s is mixed with the vacuum state $\varrho_0 = |0\rangle\langle0|$ at a beam splitter (BS) with transmissivity T; then, on/off photodetection with quantum efficiency ε is performed on the reflected beam. When the detector clicks, we obtain the IPS state ϱ_1.

properties depending on the particular test and on the choice of the involved parameters.

This paper is devoted to a review the effects of the IPS process on TWBs either in the ideal case, i.e., when the detection is not affected by losses and no dissipation or thermal noise occurs during the propagation of the involved modes, or when nonunit quantum efficiency is taken into account, as well as when the dynamics through a noisy channel is considered.

The paper is structured as follows: in the next section, we introduce photon subtraction as a method to enhance nonclassicality of a radiation state and illustrate inconclusive photon subtraction on a single-mode field. The de-Gaussification process on two-mode fields is described in Section 3, where the map of the IPS process is given both in the Fock representation and in the phase space. In Section 4, we briefly review the dynamics of a TWB in noisy channels and show that IPS can also be profitably applied in the presence of noise. The CV teleportation protocol is described in Section 5, where we compare the teleportation fidelity when the protocol is assisted and not assisted by the IPS process. In the following sections, in order to characterize in detail the nonlocal properties of the IPS states, we consider different *Bell* tests, namely, the nonlocality test in the phase space (Section 6), the homodyne detection test (Section 7), the pseudospin test (Section 8), and a nonlocality test based on on/off photodetection (Section 9). Finally, Section 10 closes the paper with some concluding remarks.

2. PHOTON SUBTRACTION

The idea of enhancing the nonclassical properties of radiation by subtraction of photons was introduced in the context of Schrodinger cat generation [20] and subsequently applied to the improvement of CV teleportation fidelity [8]. In the schemes of [8, 20] the field mode to undergo photon subtraction (PS) is impinged onto a beam-splitter with high transmissivity and whose second port is left unexcited. At the output of the beam splitter, the reflected mode undergoes photon number measurement, whereas the conditional state of the transmitted mode represents the PS state. The properties of the PS state depend on the number of detected photons, with single-photon-subtracted states playing a

major role in the enhancement of nonclassicality. Unfortunately, the realization of photon-number-resolving detectors is still experimentally challenging, and therefore a question arises concerning the experimental feasibility of subtraction schemes.

Photodetectors that are usually available in quantum optics, such as avalanche photodiodes (APDs), operate in the Geiger mode [21, 22]. They can be used to reconstruct the photon statistics [23, 24] but cannot be used as photon counters. APDs show high quantum efficiency, but their breakdown current is independent of the number of detected photons, which in turn cannot be determined. The output of these APDs is either "off" (no photons detected) or "on," i.e., a click, indicating the detection of one or more photons. Actually, such an output can be provided by any photodetector (photomultiplier, hybrid photodetector, cryogenic thermal detector) for which the charge contained in dark pulses is definitely below that of the output current pulses corresponding to the detection of at least one photon. Note that, for most high-gain photomultipliers, the anodic pulses corresponding to no photons detected can be easily discriminated by a threshold from those corresponding to the detection of one or more photons.

It appears therefore of interest to investigate the properties of photon-subtracted states when the number of detected photons is not discriminated. Such a process will be referred to as inconclusive photon subtraction (IPS) throughout the paper. The scheme of the IPS process is sketched in Fig. 1. Mode a excited in state ϱ_s is mixed with the vacuum $\varrho_0 = |0\rangle\langle0|$ (mode b) at an unbalanced beam splitter (BS) with transmissivity $T = \cos^2\phi$, and then on/off avalanche photodetection with quantum efficiency ε is performed on the reflected beam. APDs can only discriminate the presence of radiation from the vacuum. The positive operator-valued measure (POVM) $\{\Pi_0(\varepsilon), \Pi_1(\varepsilon)\}$ of the detector is given by

$$\Pi_0(\varepsilon) = \sum_{k=0}^{\infty} (1-\varepsilon)^k |k\rangle\langle k|,$$

$$\Pi_1(\varepsilon) = \mathbb{I} - \Pi_0(\varepsilon). \tag{1}$$

The whole process can be characterized by T and ε, which will be referred to as the IPS transmissivity and the IPS quantum efficiency. The conditional state of the transmitted mode after the observation of a click is given by

$$\varrho_1$$
$$= \frac{1}{p_1(\phi, \varepsilon)} \mathrm{Tr}_b [U_{ab}(\phi)\varrho_s \otimes \varrho_0 U_{ab}^\dagger(\phi) \mathbb{I}_a \otimes \Pi_1(\varepsilon)], \tag{2}$$

where $U_{ab}(\phi) = \exp\{-\phi(a^\dagger b - ab^\dagger)\}$ is the evolution operator of the beam splitter and $p_1(\phi, \varepsilon)$ is the probability of a click. In general, the transformation (2) real-

izes a nonunitary quantum operation $\varrho_1 = \mathscr{E}(\varrho_s)$ with operator-sum decomposition given by

$$\mathscr{E}(\varrho_s) = \frac{1}{p_1(\phi, \varepsilon)} \sum_{p=1}^{\infty} m_p(\phi, \varepsilon) E_p(\phi)\varrho_s E_p^{\dagger}(\phi), \quad (3)$$

where

$$m_p(\phi, \varepsilon) = \frac{\tan^{2p}\phi[1 - (1 - \varepsilon)^p]}{p!}, \quad (4)$$

$$M_p(\phi) = a^p \cos^{a^{\dagger}a}\phi, \quad (5)$$

which is found by explicit evaluation of the partial trace in (2). The IPS state obtained by applying the map (3) to a Gaussian state is no longer Gaussian, and therefore IPS represents an effective source of non-Gaussian states, which should be otherwise generated by highly nonlinear, and thus inherently low-rate, optical processes.

In general, the IPS process can produce an output state whose energy is larger than that of the input state and whose nonclassical properties can be enhanced. As an example, we address photon subtraction onto a Gaussian state described by the following Wigner function (using the Wigner function formalism makes analytical calculations more straightforward):

$$W_s(z) = \frac{\exp\{-F|z|^2 - G(z^2 + z^{*2})\}}{\pi\sqrt{(F^2 - 4G^2)^{-1}}}, \quad (6)$$

whose energy is given by

$$E_s = \int_{\mathbb{C}} d^2z\left(|z|^2 - \frac{1}{2}\right)W_s(z) = \frac{F}{F^2 - 4G^2} - \frac{1}{2}. \quad (7)$$

When state (6) undergoes the IPS process described above, the Wigner function associated with the output state ϱ_1 reads [13]

$$W_1(z) = \frac{1}{p_1(\phi, \varepsilon)} \sum_{k=1}^{2} \mathscr{C}_k(\phi, \varepsilon)W_k(z), \quad (8)$$

with $\mathscr{C}_1(\phi, \varepsilon) = 1$, $\mathscr{C}_2(\phi, \varepsilon) = -(\varepsilon\sqrt{\text{Det}[\mathbf{B} + \boldsymbol{\sigma}_M]})^{-1}$, where

$$\mathbf{B} = (1 - T)\boldsymbol{\sigma} + \frac{T}{2}\mathbb{1}_2, \quad \boldsymbol{\sigma}_M = \frac{2-\varepsilon}{2\varepsilon}\mathbb{1}_2, \quad (9)$$

where $\mathbb{1}_2$ is the 2×2 identity matrix and $\boldsymbol{\sigma}$ is the covariance associated with state (6):

$$\boldsymbol{\sigma} = \begin{pmatrix} (F + 2G)^{-1} & 0 \\ 0 & (F - 2G)^{-1} \end{pmatrix}, \quad (10)$$

where $[\boldsymbol{\sigma}]_{hk} = \frac{1}{2}\langle\{R_h, R_k\}\rangle - \langle R_h\rangle\langle R_k\rangle$, $\{A, B\} = AB + BA$ denotes the anticommutator, and

$$\mathbf{R} = (R_1, R_2)^T \equiv \left(\frac{a + a^{\dagger}}{\sqrt{2}}, \frac{a - a^{\dagger}}{i\sqrt{2}}\right)^T, \quad (11)$$

$(...)^T$ being the transposition operation. Notice that $W_1(z)$ is no longer Gaussian. In Eq. (8), we defined

$$W_k(z) = \frac{\exp\{-F_k|z|^2 - G_k(z^2 + z^{*2})\}}{\pi\sqrt{(F_k^2 - 4G_k^2)^{-1}}}, \quad (12)$$

where

$$F_1 = \mathscr{U}_+ + \mathscr{U}_-, \quad G_1 = \frac{1}{2}(\mathscr{U}_+ - \mathscr{U}_-), \quad (13)$$

$$F_2 = 2(\mathscr{V}_+ + \mathscr{V}_-), \quad G_2 = \mathscr{V}_+ - \mathscr{V}_-, \quad (14)$$

with

$$\mathscr{U}_\pm = \frac{F \pm 2G}{2T + (1 - T)(F \pm 2G)}, \quad (15)$$

$$\mathscr{V}_\pm = \frac{F + 2(1 \pm G)T}{4T + (1 - T)[2\varepsilon + (2 - \varepsilon)(F \pm 2G)]}. \quad (16)$$

Because of analytical expression (8), the energy of the photon-subtracted state is simply given by

$$E_1(T, \varepsilon) = \frac{1}{p_1(T, \varepsilon)} \sum_{k=1}^{2} \mathscr{C}_k\left[\frac{F_k}{F_k^2 - 4G_k^2} - \frac{1}{2}\right], \quad (17)$$

with $\mathscr{C}_k \equiv \mathscr{C}_k(T, \varepsilon)$ and where we put $T = \cos^2\phi$.

Let us now focus our attention on the IPS process applied to the squeezed vacuum $|0, r\rangle = S(r)|0\rangle$, where $S(r) = \exp\{r(a^{\dagger 2} - a^2)/2\}$ is the squeezing operator, which has recently been realized experimentally [11]. The Wigner function associated with $|0, r\rangle$ is given by Eq. (6) with $F = 2\cosh 2r$ and $G = -\sinh 2r$. In Fig. 2, we plot the energies E_s and E_1 of the input and output states, respectively, for different values of the involved parameters as functions of $\tanh r$. We can see that there is a threshold on r, depending on T and ε, under which the IPS state has a larger energy than the input state. Furthermore, when $\varepsilon = 1$, $T \longrightarrow 1$ and $r \longrightarrow 0$, we can see that $E_1 \longrightarrow 1$: in these limits, the output state approaches the squeezed Fock state $S(r)|1\rangle$ [12, 13]. Finally, in Fig. 3, E_1 is plotted for two values of T and different values of ε as a function of $\tanh r$: we find that, as r increases, the IPS efficiency is not so relevant in the process.

3. PHOTON SUBTRACTION ON BIPARTITE STATES

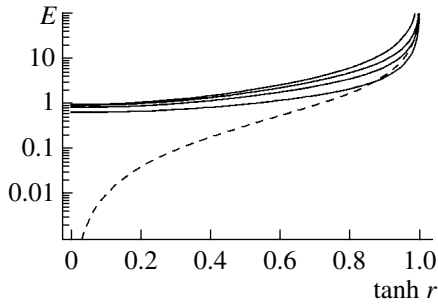In this section, we address de-Gaussification of bipartite states by IPS. The de-Gaussification can be

Fig. 2. Logarithmic plots of the energies E_s (dashed line) and E_1 (solid lines) in the case of a squeezed vacuum $|0, r\rangle$ as input state and as functions of $\tanh r$ for $\varepsilon = 1$ and different values of T. From top to bottom (solid lines): $T = 1.0$, 0.9, 0.75, and 0.5.
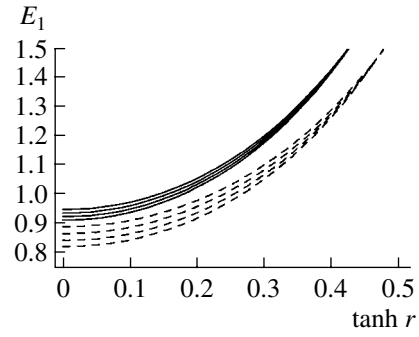

Fig. 3. Plots of the energy E_1 of the IPS state in the case of a squeezed vacuum $|0, r\rangle$ as input state as a function of $\tanh r$ for $T = 0.9$ (solid lines) and $T = 0.8$ (dashed lines) and different values of ε. From top to bottom: $\varepsilon = 1.0$, 0.75, 0.5, and 0.25.

achieved by subtracting photons from both modes through on/off detection [9, 10]. The IPS scheme for two modes is sketched in Fig. 4. The modes a and b of the shared bipartite state ϱ_s are mixed with vacuum modes at two unbalanced beam splitters (BS) with equal transmissivity $T = \cos^2\phi$; the reflected modes c and d are then revealed by avalanche photodetectors (APD) with equal efficiency ε. The conditional measurement on modes c and d is described by the POVM (assuming equal quantum efficiency for the photodetectors)

$$\Pi_{00}(\varepsilon) = \Pi_{0,\,c}(\varepsilon) \otimes \Pi_{0,\,d}(\varepsilon), \tag{18}$$

$$\Pi_{01}(\varepsilon) = \Pi_{0,\,c}(\varepsilon) \otimes \Pi_{1,\,d}(\varepsilon), \tag{19}$$

$$\Pi_{10}(\varepsilon) = \Pi_{1,\,c}(\varepsilon) \otimes \Pi_{0,\,d}(\varepsilon), \tag{20}$$

$$\Pi_{11}(\varepsilon) = \Pi_{1,\,c}(\varepsilon) \otimes \Pi_{1,\,d}(\varepsilon). \tag{21}$$

When the two photodetectors jointly click, the conditioned output state of modes a and b is given by [10, 14]

$$\mathscr{E}(\varrho_s) = \frac{\mathrm{Tr}_{cd}[U_{ac}(\phi) \otimes U_{bd}(\phi)\varrho_s \otimes |0\rangle_{cddc}\langle 0|U_{ac}^\dagger(\phi) \otimes U_{bd}^\dagger(\phi)\mathbb{I}_a \otimes \mathbb{I}_b \otimes \Pi_{11}(\varepsilon)]}{p_{11}(r, \phi, \varepsilon)}, \tag{22}$$

where $U_{ac}(\phi) = \exp\{-\phi(a^\dagger c - ac^\dagger)\}$ and $U_{bd}(\phi)$ are the evolution operators of the beam splitters, $|0\rangle_{cd} \equiv |0\rangle_c \otimes |0\rangle_d$, and $p_{11}(r, \phi, \varepsilon)$ is the probability of a click in both detectors. The partial trace on modes c and d can be explicitly evaluated, thus arriving at the following decomposition of the IPS map:

$$\mathscr{E}(\varrho_s) = \frac{1}{p_{11}(r, \phi, \varepsilon)} \tag{23}$$
$$\times \sum_{p,\,q=1}^\infty m_p(\phi, \varepsilon) M_{pq}(\phi)\varrho_s M_{pq}^\dagger(\phi) m_q(\phi, \varepsilon),$$

where

$$M_{pq}(\phi) = a^p b^q (\cos\phi)^{a^\dagger a + b^\dagger b}. \tag{24}$$

Equation (23) is indeed an operator-sum representation of the IPS map: $\{p, q\} \equiv \theta$ should be intended as a poly-index, so that expression (23) reads $\mathscr{E}(\varrho_s) = \sum_\theta A_\theta \varrho_s A_\theta^\dagger$ with $A_\theta = [p_{11}(r, \phi, \varepsilon)]^{-1/2} m_p(\phi, \varepsilon) M_{pq}(\phi)$.

From now on, we focus our attention on the case in which the shared state is the twin-beam state of radiation (TWB) $\varrho_s = |\Lambda\rangle\rangle\langle\langle\Lambda|$, where $|\Lambda\rangle\rangle = \sqrt{1-\lambda^2}\sum_k \lambda^k |k\rangle \otimes |k\rangle$ with $\lambda = \tanh r$, r being the TWB squeezing parameter. The TWB is obtained by parametric downconversion of the vacuum, $|\Lambda\rangle\rangle = \exp\{r(a^\dagger b^\dagger - ab)\}|0\rangle$, a and b being field operators, and it is described by the Gaussian Wigner function

$$W_0(\alpha, \beta)$$
$$= \frac{\exp\{-2\tilde{A}_0(|\alpha|^2 + |\beta|^2) + 2\tilde{B}_0(\alpha\beta + \alpha^*\beta^*)\}}{\pi^2\sqrt{\mathrm{Det}[\boldsymbol{\sigma}_0]}}, \tag{25}$$

with

$$\tilde{A}_0 = \frac{A_0}{4\sqrt{\mathrm{Det}[\boldsymbol{\sigma}_0]}}, \quad \tilde{B}_0 = \frac{B_0}{4\sqrt{\mathrm{Det}[\boldsymbol{\sigma}_0]}}, \tag{26}$$

where $A_0 \equiv A_0(r) = \cosh(2r)$, $B_0 \equiv B_0(r) = \sinh(2r)$ and $\boldsymbol{\sigma}_0$ is the covariance matrix

$$\boldsymbol{\sigma}_0 = \frac{1}{2}\begin{pmatrix} A_0 1_2 & B_0\boldsymbol{\sigma}_3 \\ B_0\boldsymbol{\sigma}_3 & A_0 1_2 \end{pmatrix}, \qquad (27)$$

where 1_2 is the 2×2 identity matrix and $\boldsymbol{\sigma}_3 = \mathrm{Diag}(1, -1)$; $\boldsymbol{\sigma}_0$ is defined as $[\boldsymbol{\sigma}_0]_{hk} = \frac{1}{2}\langle\{R_h, R_k\}\rangle - \langle R_h\rangle\langle R_k\rangle$, with

$$\mathbf{R} = (R_1, R_2, R_3, R_4)^T \qquad (28)$$

$$\equiv \left(\frac{a+a^\dagger}{\sqrt{2}}, \frac{a-a^\dagger}{i\sqrt{2}}, \frac{b+b^\dagger}{\sqrt{2}}, \frac{b-b^\dagger}{i\sqrt{2}}\right)^T. \qquad (29)$$

Now we explicitly calculate the Wigner function of the corresponding IPS state, which, as one may expect, is no longer Gaussian and positive definite. The state entering the two beam splitters is described by the Wigner function

$$W_0^{(\mathrm{in})}(\alpha, \beta, \zeta, \xi)$$
$$= W_0(\alpha, \beta)\frac{4}{\pi^2}\exp\{-2|\zeta|^2 - 2|\xi|^2\}, \qquad (30)$$

where the second factor on the right-hand side represents the two vacuum states of modes c and d. The action of the beam splitters on $W_r^{(\mathrm{in})}$ can be summarized by the following change of variables [2]:

$$\alpha \longrightarrow \alpha\cos\phi + \zeta\sin\phi, \quad \zeta \longrightarrow \zeta\cos\phi - \alpha\sin\phi, \quad (31)$$

$$\beta \longrightarrow \beta\cos\phi + \xi\sin\phi, \quad \xi \longrightarrow \xi\cos\phi - \beta\sin\phi, \quad (32)$$

and the output state, after the beam splitters, is then given by

$$W_{r,\phi}^{(\mathrm{out})}(\alpha, \beta, \zeta, \xi)$$
$$= \frac{4}{\pi^2}W_{r,\phi}(\alpha, \beta)\exp\{-a|\xi|^2 + w\xi + w^*\xi^*\}$$
$$\times \exp\{-a|\zeta|^2 + (v + 2\tilde{B}_0\xi\sin^2\phi)\zeta$$
$$+ (v^* + 2\tilde{B}_0\xi^*\sin^2\phi)\zeta^*\}, \qquad (33)$$

where

$$W_{r,\phi}(\alpha, \beta)$$
$$= \frac{\exp\{-b(|\alpha|^2 + |\beta|^2) + 2\tilde{B}_0\cos^2\phi(\alpha\beta + \alpha^*\beta^*)\}}{\pi^2\sqrt{\mathrm{Det}[\boldsymbol{\sigma}_0]}} \qquad (34)$$

and

$$a \equiv a(r, \phi) = 2(\tilde{A}_0\sin^2\phi + \cos^2\phi), \qquad (35)$$

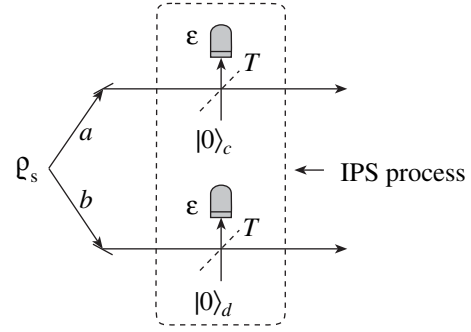$$b \equiv b(r, \phi) = 2(\tilde{A}_0\cos^2\phi + \sin^2\phi), \qquad (36)$$

Fig. 4. Scheme of the IPS process. The two modes, a and b, of a shared bipartite state ϱ_s are mixed with the vacuum at two BSs with equal transmissivity T and on/off photodetection with quantum efficiency ε is performed on the reflected beam: when both the detectors click, one obtains the IPS state.

$$v \equiv v(r, \phi) = 2\cos\phi\sin\phi[(1 - \tilde{A}_0)\alpha^* + \tilde{B}_0\beta], \quad (37)$$

$$w \equiv w(r, \phi) = 2\cos\phi\sin\phi[(1 - \tilde{A}_0)\beta^* + \tilde{B}_0\alpha]. \quad (38)$$

At this stage, on/off detection is performed on modes c and d (see Fig. 4). We are interested in the situation when both the detectors click. The Wigner function of the double-click element $\Pi_{11}(\varepsilon)$ of the POVM [see Eq. (21)] is given by [10, 28]

$$W_\varepsilon(\zeta, \xi) \equiv W[\Pi_{11}(\varepsilon)](\zeta, \xi) \qquad (39)$$

$$= \frac{1}{\pi^2}\{1 - Q_\varepsilon(\zeta) - Q_\varepsilon(\xi) + Q_\varepsilon(\zeta)Q_\varepsilon(\xi)\}, \qquad (40)$$

with

$$Q_\varepsilon(z) = \frac{2}{2-\varepsilon}\exp\left\{-\frac{2\varepsilon}{2-\varepsilon}|z|^2\right\}. \qquad (41)$$

Using Eq. (22) and the phase-space expression of the trace for each mode, i.e.,

$$\mathrm{Tr}[O_1 O_2] = \pi\int_{\mathbb{C}} d^2z\, W[O_1](z)W[O_2](z), \qquad (42)$$

we find that the Wigner function of the output state, conditioned to the double-click event, is

$$W_{r,\phi,\varepsilon}(\alpha, \beta) = \frac{f(\alpha, \beta)}{p_{11}(r, \phi, \varepsilon)}, \qquad (43)$$

where $f(\alpha, \beta) = f_{r,\phi,\varepsilon}(\alpha, \beta)$ with

$$f(\alpha, \beta) = \pi^2\int_{\mathbb{C}^2} d^2\zeta d^2\xi\frac{4}{\pi^2}W_{r,\phi}(\alpha, \beta)$$
$$\times \sum_{k=1}^{4}\frac{C_k}{\pi^2}G_{r,\phi,\varepsilon}^{(k)}(\alpha, \beta, \zeta, \xi), \qquad (44)$$
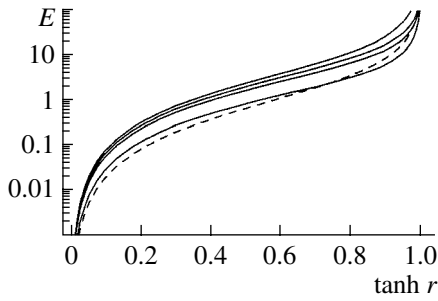
Fig. 5. Logarithmic plots of the energies E_s (dashed line) and E_{IPS} (solid lines) in the case of a TWB as input state as functions of tanh r for $\varepsilon = 1$ and different values of T. From top to bottom (solid lines): $T = 1.0, 0.9, 0.75,$ and 0.5.

where $C_k \equiv C_k(\varepsilon)$ and $C_1 = 1$, $C_2 = C_3 = -2(2-\varepsilon)^{-1}$, $C_4 = 4(2-\varepsilon)^{-2}$. The double-click probability $p_{11}(r, \phi, \varepsilon)$ can be written as a function of $f(\alpha, \beta)$ as follows:

$$p_{11}(r, \phi, \varepsilon) = \pi^2 \int_{\mathbb{C}^2} d^2\alpha d^2\beta f(\alpha, \beta). \qquad (45)$$

The quantities $G_{r, \phi, \varepsilon}^{(k)}(\alpha, \beta, \zeta, \xi)$ in Eq. (44) are given by

$$G_{r, \phi, \varepsilon}^{(k)}(\alpha, \beta, \zeta, \xi)$$
$$= \exp\{-x_k|\zeta|^2 + (v + 2B\xi \sin^2\phi)\zeta \qquad (46)$$
$$+ (v^* + 2B\xi^* \sin^2\phi)\zeta^*\}$$
$$\times \exp\{-y_k|\xi|^2 + w\xi + w^*\xi^*\},$$

where $x_k \equiv x_k(r, \phi, \varepsilon)$, and $y_k \equiv y_k(r, \phi, \varepsilon)$ are

$$x_1 = x_3 = y_1 = y_2 = a,$$

$$x_2 = x_4 = y_3 = y_4 = a + 2\varepsilon(2-\varepsilon)^{-1}.$$

After the integrations, we have

$$f(\alpha, \beta) = \frac{1}{\pi^2} \sum_{k=1}^{4} \mathscr{C}_k \exp\{(f_k - b)|\alpha|^2 + (g_k - b)|\beta|^2$$
$$+ (2\tilde{B}_0 T + h_k)(\alpha\beta + \alpha^*\beta^*)\} \qquad (47)$$

and

$$p_{11}(r, T, \varepsilon) = \sum_{k=1}^{4} \frac{\mathscr{C}_k}{(b - f_k)(b - g_k) - (2\tilde{B}_0 T + h_k)^2}, \qquad (48)$$

where we put $T = \cos^2\phi = 1 - \sin^2\phi$ and defined

$$\mathscr{C}_k \equiv \mathscr{C}_k(r, T, \varepsilon) = \frac{4C_k}{[x_k y_k - 4\tilde{B}_0^2(1-T)^2]\sqrt{\text{Det}[\boldsymbol{\sigma}_0]}} \qquad (49)$$

and $f_k \equiv f_k(r, T)$, $g_k = g_k(r, T)$, and $h_k \equiv h_k(r, T)$ given by

$$f_k = \mathcal{N}_k[x_k\tilde{B}_0^2 + 4\tilde{B}_0^2(1 - \tilde{A}_0)(1 - T) \qquad (50)$$
$$+ y_k(1 - \tilde{A}_0)^2],$$

$$g_k = \mathcal{N}_k[x_k(1 - \tilde{A}_0)^2 \qquad (51)$$
$$+ 4\tilde{B}_0^2(1 - \tilde{A}_0)(1 - T) + y_k\tilde{B}_0^2],$$

$$h_k = \mathcal{N}_k\{(x_k + y_k)\tilde{B}_0(1 - \tilde{A}_0)$$
$$+ 2\tilde{B}_0[\tilde{B}_0^2 + (1 - \tilde{A}_0)^2](1 - T)\}, \qquad (52)$$

$$\mathcal{N}_k \equiv \mathcal{N}_k(r, T) = \frac{4T(1 - T)}{x_k y_k - 4\tilde{B}_0^2(1 - T)^2}. \qquad (53)$$

In this way, the Wigner function of the IPS state can be rewritten as

$$W_{IPS}(\alpha, \beta) = \frac{1}{\pi^2 p_{11}(r, T, \varepsilon)} \sum_{k=1}^{4} \mathscr{C}_k W_k(\alpha, \beta), \quad (54)$$

with

$$W_k(\alpha, \beta) = \exp\{(f_k - b)|\alpha|^2 + (g_k - b)|\beta|^2 \qquad (55)$$
$$+ (2\tilde{B}_0 T + h_k)(\alpha\beta + \alpha^*\beta^*)\}.$$

Finally, the density matrix corresponding to $W_{IPS}(\alpha, \beta)$ reads as follows [10]:

$$\varrho_{IPS} = \frac{1 - \lambda^2}{p_{11}(r, T, \varepsilon)} \sum_{n, m = 0}^{\infty} (\lambda T)^{n+m} \sum_{h, k = 0}^{\text{Min}[n, m]} \mathscr{A}_{h, k}(T, \varepsilon)$$
$$\times \sqrt{\frac{n}{h}\frac{n}{k}\frac{m}{h}\frac{m}{k}} |n - k\rangle_a |n - h\rangle_{bb}\langle m - h|_a\langle m - k|, \qquad (56)$$

where $\lambda = \tanh r$ and

$$\mathscr{A}_{h, k}(T, \varepsilon)$$
$$= [1 - (1-\varepsilon)^h][1 - (1-\varepsilon)^k]\left(\frac{1-T}{T}\right)^{h+k}. \qquad (57)$$

In Fig. 5, we plot the energies E_s and E_{IPS} of the bipartite input and output states, respectively, for different values of the involved parameters as functions of tanh r. We recall that, for a given Wigner function $W(v, w)$ of a bipartite state, the corresponding energy is

$$E = \int_{\mathbb{C}^2} d^2v d^2w (|v|^2 + |w|^2 - 1)W(v, w). \qquad (58)$$

If the bipartite state has a Wigner function of the form

$$W_s(v, w)$$
$$= \frac{\exp\{-F|v|^2 - G|w|^2 + H(vw + v^*w^*)\}}{\pi^2(FG - H^2)^{-1}}, \qquad (59)$$

then its energy is

$$E_s = \frac{F + G}{2(FG - H^2)} - 1. \tag{60}$$

Thereby, in the case of a TWB as input state, F, G, and H are obtained from Eq. (25) and the energy of the state emerging from the IPS process can be written as

$$E_{IPS} = \frac{1}{\pi^2 p_{11}(r, T, \varepsilon)} \sum_{k=1}^{4} \mathscr{C}_k \left[\frac{F_k + G_k}{2(F_k G_k - H_k^2)^2} - 1 \right], \tag{61}$$

with $F_k = b - f_h$, $G_k = b - g_h$, and $H_k = 2\tilde{B}_0 T + h_k$, and all the involved quantities are the same as in Eq. (54). As in the single-mode case, we can see that there is a threshold on r, depending on T and ε, under which the IPS state has a larger energy than the input state. In Fig. 6, E_{IPS} is plotted for two values of T and different values of ε as a function of tanh r: we find that, as r decreases, the IPS efficiency is not so relevant.

The state given in Eq. (54) is no longer a Gaussian state, and its use in the improvement of continuous variable teleportation [10], as well as in the enhancement of the nonlocality [14, 16, 17], will be investigated in the following sections.

4. DYNAMICS OF TWB IN NOISY CHANNELS

Before addressing the properties of the IPS bipartite state described in the previous section, we review the evolution of the twin-beam state of radiation (TWB) in a noisy environment, namely, an environment where dissipation and thermal noise take place [15]. As we will see, we can include in our analysis the effect due to the propagation through this kind of channel by a simple change of the involved quantities. Using a more compact form, Eq. (25) can also be rewritten as

$$W_0(\mathbf{X}) = \frac{\exp\left\{-\frac{1}{2}\mathbf{X}^T\boldsymbol{\sigma}_0^{-1}\mathbf{X}\right\}}{\pi^2\sqrt{\text{Det}[\boldsymbol{\sigma}_0]}}, \tag{62}$$

with $\mathbf{X} = (x_1, y_1, x_2, y_2)^T$, $\alpha = \frac{1}{\sqrt{2}}(x_1 + iy_1)$ and $\beta = \frac{1}{\sqrt{2}}(x_2 + iy_2)$, and $(\dots)^T$ denoting the transposition operation.

When the two modes of the TWB interact with a noisy environment, namely, in the presence of dissipation and thermal noise, the evolution of Wigner function (25) is described by the following Fokker-Planck equation [25–27]:

$$\partial_t W_t(\mathbf{X}) = \frac{1}{2}(\partial_{\mathbf{X}}^T \boldsymbol{\Gamma}\mathbf{X} + \partial_{\mathbf{X}}^T \boldsymbol{\Gamma}\boldsymbol{\sigma}_\infty\partial_{\mathbf{X}})W_t(\mathbf{X}), \tag{63}$$

with $\partial_{\mathbf{X}} = (\partial_{x_1}, \partial_{y_1}, \partial_{x_2}, \partial_{y_2})^T$. The damping matrix is given by $\boldsymbol{\Gamma} = \bigoplus_{k=1}^{2} \Gamma_k \mathbf{1}_2$, whereas

$$\boldsymbol{\sigma}_\infty = \bigoplus_{k=1}^{2} \boldsymbol{\sigma}_\infty^{(k)} = \begin{pmatrix} \boldsymbol{\sigma}_\infty^{(1)} & \mathbf{0} \\ \mathbf{0} & \boldsymbol{\sigma}_\infty^{(2)} \end{pmatrix}, \tag{64}$$

where $\mathbf{0}$ is the 2×2 null matrix and

$$\boldsymbol{\sigma}_\infty^{(k)} = \frac{1}{2}\begin{pmatrix} 1 + 2N_k & 0 \\ 0 & 1 + 2N_k \end{pmatrix}. \tag{65}$$

Here, Γ_k and N_k denote the damping rate and the average number of thermal photons of the channel k, respectively, and $\boldsymbol{\sigma}_\infty$ represents the covariance matrix of the environment and, in turn, the asymptotic covariance matrix of the evolved TWB. Since the environment is itself excited in a Gaussian state, the evolution induced by expression (63) preserves the Gaussian form (62). The covariance matrix at time t reads as follows [2, 27]:

$$\boldsymbol{\sigma}_t = G_t^{1/2}\boldsymbol{\sigma}_0 G_t^{1/2} + (1 - G_t)\boldsymbol{\sigma}_\infty, \tag{66}$$

where $G_t = \bigoplus_{k=1}^{2} e^{-\Gamma_k t}\mathbf{1}_2$. The covariance matrix $\boldsymbol{\sigma}_t$ can be also written as

$$\boldsymbol{\sigma}_t = \frac{1}{2}\begin{pmatrix} A_t(\Gamma_1, N_1)\mathbf{1}_2 & B_t(\Gamma_1)\boldsymbol{\sigma}_3 \\ B_t(\Gamma_2)\boldsymbol{\sigma}_3 & A_t(\Gamma_2, N_2)\mathbf{1}_2 \end{pmatrix}, \tag{67}$$

with

$$A_t(\Gamma_k, N_k) = A_0 e^{-\Gamma_k t} + (1 - e^{-\Gamma_k t})(1 + 2N_k),$$
$$B_t(\Gamma_k) = B_0 e^{-\Gamma_k t}. \tag{68}$$

Finally, if we assume $\Gamma_1 = \Gamma_2 = \Gamma$ and $N_1 = N_2 = N$, then the covariance matrix (67) becomes formally identical to (27), and the corresponding Wigner function reads

$$W_t(\alpha, \beta)$$
$$= \frac{\exp\{-2\tilde{A}_t(|\alpha|^2 + |\beta|^2) + 2\tilde{B}_t(\alpha\beta + \alpha^*\beta^*)\}}{\pi^2\sqrt{\text{Det}[\boldsymbol{\sigma}_t]}}, \tag{69}$$

with

$$\tilde{A}_t = \frac{A_t(\Gamma, N)}{4\sqrt{\text{Det}[\boldsymbol{\sigma}_t]}}, \quad \tilde{B}_t = \frac{B_t(\Gamma)}{4\sqrt{\text{Det}[\boldsymbol{\sigma}_t]}}. \tag{70}$$

If the IPS process is performed on a TWB evolved in a noisy environment with both the channels having the same damping rate and thermal noise, then the Wigner function of the state arriving at the beam splitters is now given by Eq. (69), and the output state is still
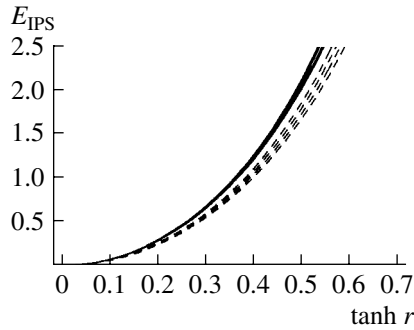
Fig. 6. Plots of the energy E_{IPS} of the IPS state in the case of the TWB as input state as a function of $\tanh r$ for $T = 0.9$ (solid lines) and $T = 0.8$ (dashed lines) and different values of ε. From top to bottom: $\varepsilon = 1.0, 0.75, 0.5,$ and 0.25.

Fig. 7. Scheme of the CV teleportation. One of the two modes of a shared bipartite state ϱ_s is mixed with the input state ϱ_{in} at a balanced BS, and then a double-homodyne detection is performed on the two output modes measuring the complex outcome ξ. The output state ϱ_{out} is obtained displacing by the same amount ξ the remaining mode of the shared state and averaging over all the possible outcomes.

described by Eq. (54) but with the following substitutions:

$$\tilde{A}_0 \longrightarrow \tilde{A}_t, \quad \tilde{B}_0 \longrightarrow \tilde{B}_t, \quad \boldsymbol{\sigma}_0 \longrightarrow \boldsymbol{\sigma}_t. \quad (71)$$

5. CONTINUOUS VARIABLE TELEPORTATION

The scheme of continuous variable (CV) teleportation is sketched in Fig. 7. A bipartite state W_s is shared between two parties: one mode of the state is mixed at a balanced beam splitter (BS) with the state to be teleported, W_{in}, then double-homodyne measurement is performed on the two emerging modes. The complex outcome ξ of the measurement is used in order to displace the remaining mode of W_s, and the teleported state W_{out} is obtained by averaging over all the possible outcomes. Here we address the teleportation of the coherent state $|\alpha\rangle$, whose Wigner function reads

$$W_{in}(z) = \frac{2}{\pi}\exp\{-2|z - \alpha|^2\}. \quad (72)$$

If we consider the generic shared state

$$W_s(v, w)$$
$$= \frac{\exp\{-F|v|^2 - G|w|^2 + H(vw + v^*w^*)\}}{\pi^2(FG - H^2)^{-1}}, \quad (73)$$

and since the POVM describing the double homodyne detection is

$$W_\xi(z, v) = \frac{1}{\pi^2}\delta^{(2)}(z - v^* - \xi), \quad (74)$$

$\delta^{(2)}(\zeta)$ being the complex Dirac's delta function, then the output state W_{out} is given by [2]

$$W_{out}(w) = \pi^2\int_{\mathbb{C}}d^2\xi\int_{\mathbb{C}^2}d^2z\,d^2v\,W_{in}(z)$$
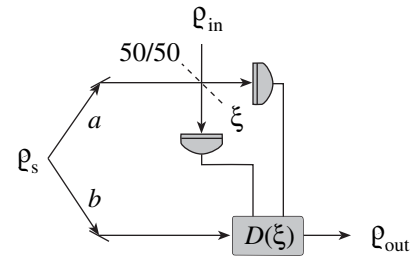$$\times W_s(v, w - \xi)W_\xi(z, v) \quad (75)$$

$$= \frac{1}{\pi\sigma_{out}}\exp\left\{-\frac{|w - \alpha|^2}{\sigma_{out}}\right\}, \quad (76)$$

where

$$\sigma_{out} = \frac{1}{2} + \frac{F + G + 2H}{FG - H^2}. \quad (77)$$

In turn, the average fidelity of teleportation of coherent states reads as follows:

$$\bar{F} \equiv \pi\int_{\mathbb{C}}d^2w\,W_{in}(w)\,W_{out}(w) \quad (78)$$

$$= \frac{FG - H^2}{FG - H^2 + F + G - 2H} = \frac{2}{1 + 2\sigma_{out}}. \quad (79)$$

When the shared state is the TWB of Eq. (25), the average fidelity is obtained from Eq. (78) with $F = G = 2\tilde{A}_0$ and $H = 2\tilde{B}_0$, i.e.,

$$\bar{F}_{TWB}(\lambda) = \frac{1}{2}(1 + \lambda), \quad (80)$$

whereas, in the presence of noise, one should use substitutions (71). $\bar{F}_{TWB}$ is plotted in Fig. 8. When the teleportation is assisted by IPS, then the fidelity reads as follows:

$$\bar{F}_{IPS} = \frac{1}{p_{11}(r, T, \varepsilon)}\sum_{k=1}^{4}\frac{\mathscr{C}_k}{F_kG_k - H_k^2 + F_k + G_k - 2H_k}, (81)$$

with $F_k = b - f_h$, $G_k = b - g_h$, and $H_k = 2\tilde{B}_0 T + h_k$, and all the involved quantities are the same as in Eq. (54). The results are presented in Fig. 9 for $\varepsilon = 1$ and $\Gamma t = N = 0$. The IPS state improves the average fidelity of quantum teleportation when λ is below a certain threshold, which depends on T (and ε). Notice that, for $T < 0.5$, $\bar{F}_{IPS}(\lambda)$ is always below $\bar{F}_{TWB}(\lambda)$, at least for $\varepsilon = 1$. The

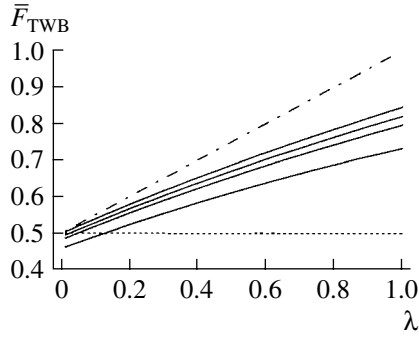**Fig. 8.** Plots of the teleportation fidelity $\bar{F}_{\text{TWB}}$ assisted by TWB in the ideal case ($\Gamma t = N = 0$, dot–dashed line) as a function of $\lambda = \tanh r$. The solid lines are $\bar{F}_{\text{TWB}}$ with $\Gamma t = 0.2$ and, from top to bottom, $N = 0, 0.1, 0.2$, and 0.5.
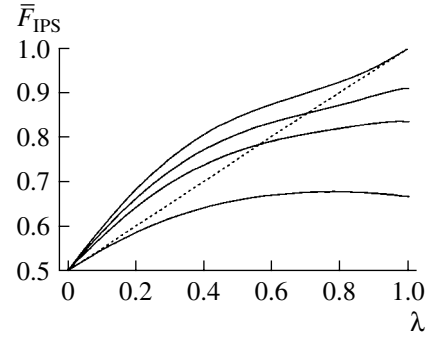

Fig. 9. Plots of the teleportation fidelity $\bar{F}_{\text{IPS}}$ assisted by IPS in the ideal case ($\Gamma t = N = 0$) as a function of $\lambda = \tanh r$. The dashed line is $\bar{F}_{\text{TWB}}$, whereas the solid lines are $\bar{F}_{\text{IPS}}$ with $\varepsilon = 1$ and, from top to bottom, $T = 1.0, 0.9, 0.8$, and 0.5.
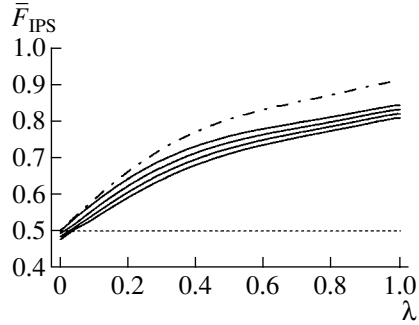
Fig. 10. Plots of the teleportation fidelity $\bar{F}_{\text{IPS}}$ assisted by IPS as a function of $\lambda = \tanh r$ with $T = 0.9$, $\varepsilon = 1$. $\Gamma t = 0.1$ and different values of N (solid lines): from top to bottom, $N = 0, 0.1, 0.2$, and 0.3. The dot–dashed line is $\bar{F}_{\text{IPS}}$ with $T = 0.9$, $\varepsilon = 1$, and $\Gamma t = N = 0$.
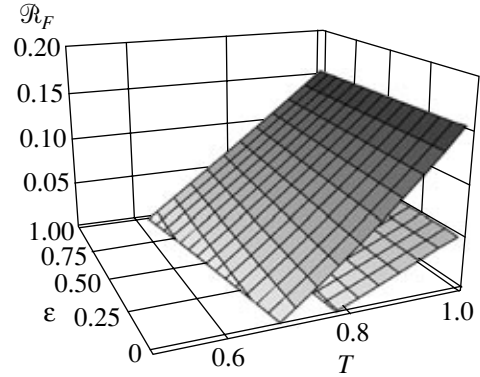

Fig. 11. Plots of $\mathcal{R}_F$ as a function of T and ε with $r = 0.3$; we set $\Gamma t = N = 0$ (upper surface) and $\Gamma t = N = 0.1$ (lower surface). $\mathcal{R}_F$ and, in turn, $\bar{F}_{\text{IPS}}$ is mainly affected by the IPS transmissivity T.

effect of dissipation and thermal noise is shown in Fig. 10.

In order to quantify the improvement and to study its dependence on T and ε, we define the following "relative improvement":

$$\mathcal{R}_F(r, T, \varepsilon, \Gamma, N)$$
$$= \frac{\bar{F}_{\text{IPS}}(r, T, \varepsilon, \Gamma, N) - \bar{F}_{\text{TWB}}(r, \Gamma, N)}{\bar{F}_{\text{TWB}}(r, \Gamma, N)}, \quad (82)$$

which is plotted in Fig. 11 we can see that $\mathcal{R}_F$ and, in turn, $\bar{F}_{\text{IPS}}$ are mainly affected by T when Γt and N are fixed. In Fig. 12, we plot $\mathcal{R}_F$ as a function $\lambda = \tanh r$ and the quantity $\mathcal{R}_F^{(\text{id})}$ defined as follows:

$$\mathcal{R}_F^{(\text{id})}(r, T, \varepsilon, \Gamma, N)$$
$$= \frac{\bar{F}_{\text{IPS}}(r, T, \varepsilon, \Gamma, N) - \bar{F}_{\text{TWB}}(r, 0, 0)}{\bar{F}_{\text{TWB}}(r, 0, 0)}, \quad (83)$$

i.e., the relative improvement of the fidelity using IPS in the presence of losses and thermal noise with respect to the fidelity using the TWB in ideal conditions ($\Gamma t = N = 0$). We can see that, for the particular choice of the parameters, not only is the fidelity improved with respect to the TWB-based teleportation in the presence of the same dissipation and thermal noise (solid line in Fig. 12), but the results can also be better than the ideal case (dot–dashed line). We can conclude that IPS onto TWB degraded by dissipation and noisy environment can improve the fidelity of teleportation up to and beyond the value achievable using the TWB in ideal conditions.

Finally, in Fig. 13, we plot the teleportation fidelity as a function of the average number of photons N of the shared state in the case of TWB and a photon-subtracted TWB: we can see that, for a fixed energy of the shared quantum channel, the best fidelity is achieved by the TWB state. The same result holds in the presence of dissipation and thermal noise.
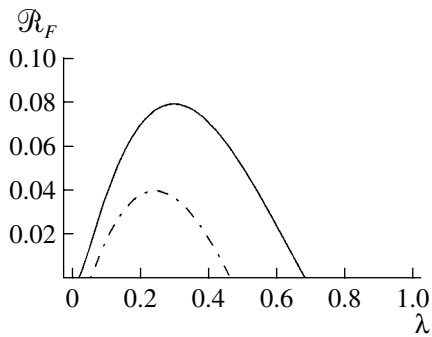
Fig. 12. Plot of the relative enhancement $\mathscr{R}_F$ as a function of $\lambda = \tanh r$ with $T = 0.9$, $\varepsilon = 1$, and $\Gamma t = N = 0.1$ (solid line). The dot–dashed line is $\mathscr{R}_F^{(\mathrm{id})}$, namely, the relative enhancement of the fidelity using the de-Gaussified TWB in a noisy environment with respect to the fidelity using TWB in the ideal case (see text for details): for a suitable choice of the parameters, the teleportation assisted by IPS in the presence of dissipation and thermal noise can have a fidelity larger than that of TWB-assisted teleportation when this is implemented under ideal conditions (i.e., $\Gamma t = N = 0$).
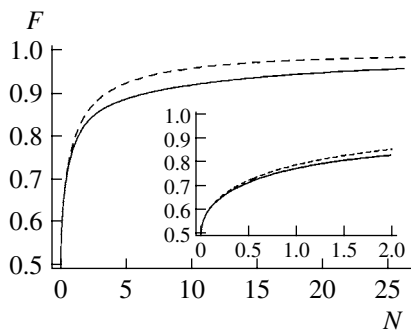

Fig. 13. Plot of the teleportation fidelity as a function of the average number of photons N of the shared state in the case of TWB (dashed line) and a photon-subtracted TWB (solid line) for $T = 0.999$, $\varepsilon = 1$, and under ideal conditions (i.e., $\Gamma t = N = 0$). The inset is a magnification of the region $0 < N < 2$.

In the next sections, we will analyze the nonlocality of the IPS state in the presence of noise by means of Bell's inequalities [15].

6. NONLOCALITY IN THE PHASE SPACE

Parity is a dichotomic variable and can thus be used to establish Bell-like inequalities [29]. The displaced parity operator on two modes is defined as [30]

$$
\begin{aligned}
&\hat{\Pi}(\alpha, \beta) \\
&= D_a(\alpha)(-1)^{a^\dagger a} D_a^\dagger(\alpha) \otimes D_b(\beta)(-1)^{b^\dagger b} D_b^\dagger(\beta),
\end{aligned}
\tag{84}
$$

where α, $\beta \in \mathbb{C}$, a and b are mode operators and $D_a(\alpha) = \exp\{\alpha a^\dagger - \alpha^* a\}$ and $D_b(\beta)$ are single-mode

displacement operators. Since the two-mode Wigner function $W(\alpha, \beta)$ can be expressed as [2]

$$
W(\alpha, \beta) = \frac{4}{\pi^2}\Pi(\alpha, \beta),
\tag{85}
$$

$\Pi(\alpha, \beta)$ being the expectation value of $\hat{\Pi}(\alpha, \beta)$, the violation of these inequalities is also known as nonlocality in the phase space. The quantity involved in such inequalities can be written as follows:

$$
\begin{aligned}
\mathscr{B}_{\mathrm{DP}} &= \Pi(\alpha_1, \beta_1) + \Pi(\alpha_2, \beta_1) \\
&\quad + \Pi(\alpha_1, \beta_2) - \Pi(\alpha_2, \beta_2),
\end{aligned}
\tag{86}
$$

which, for local theories, satisfies $|\mathscr{B}_{\mathrm{DP}}| \leq 2$.

Following [30], one can choose a particular set of displaced parity operators, arriving at the following combination [31]:

$$
\begin{aligned}
\mathscr{B}_{\mathrm{DP}}(\mathscr{J}) &= \Pi(\sqrt{\mathscr{J}}, -\sqrt{\mathscr{J}}) + \Pi(-3\sqrt{\mathscr{J}}, -\sqrt{\mathscr{J}}) \\
&\quad + \Pi(\sqrt{\mathscr{J}}, 3\sqrt{\mathscr{J}}) - \Pi(-3\sqrt{\mathscr{J}}, 3\sqrt{\mathscr{J}}),
\end{aligned}
\tag{87}
$$

which, for the TWB, gives a maximum $\mathscr{B}_{\mathrm{DP}} = 2.32$ (for $\mathscr{J} = 1.6 \times 10^{-3}$) greater than the value 2.19 obtained in [30]. Notice that, even in the infinite squeezing limit, the violation is never maximal, i.e., $|\mathscr{B}_{\mathrm{DP}}| < 2\sqrt{2}$ [32].

In [31] we studied Eq. (87) for both the TWB and the IPS state in an ideal scenario, namely, in the absence of dissipation and noise; we showed that, using IPS, the maximum violation is achieved for $T, \varepsilon \longrightarrow 1$ and for values of r smaller than for the TWB.

Now, by means of Eq. (54) and substitutions (71), we can study how noise affects $\mathscr{B}_{\mathrm{DP}}$. The results are shown in Fig. 14 for $\varepsilon = 1$: as one may expect, the overall effect of noise is to reduce the violation of Bell's inequality. When dissipation alone is present ($N = 0$), the maximum of violation is achieved using the IPS for values of r smaller than for the TWB, as in the ideal case. On the other hand, one can see that the presence of thermal noise mainly affects the IPS results. In fact, for $\Gamma t = 0.01$ and $N = 0.2$, one has $\left|\mathscr{B}_{\mathrm{DP}}^{(\mathrm{TWB})}\right| > 2$ for a range of r values, whereas $\left|\mathscr{B}_{\mathrm{DP}}^{(\mathrm{IPS})}\right|$ falls below the threshold for violation. Note that the maximum of violation, both for the TWB and the IPS state, depends on the squeezing parameter r.

In Fig. 15, we plot $\mathscr{B}_{\mathrm{DP}}^{(\mathrm{IPS})}$ as a function of T and ε. We can see that the main contribution to the Bell parameter is due to the transmissivity T. Moreover, as $T \longrightarrow 1$, the Bell parameter is actually independent of ε. Note that the values of $\mathscr{J}$ and r, which maximize the violation, depend on Γt and N, as one can see from Fig. 14. In Fig. 15, we have chosen to fix the environmental parameters in order to compare the two plots,

even if the best results can be obtained by maximizing $\mathscr{B}_{DP}^{(IPS)}$ with respect $\mathscr{J}$ and T.

We conclude that, considering the displaced parity test in the presence of noise, the IPS is quite robust if the thermal noise is below a threshold value (depending on the environmental parameters) and for small values of the TWB parameter r.

7. NONLOCALITY AND HOMODYNE DETECTION

In principle, there are two approaches to testing the Bell inequalities for a bipartite state: either one can employ some test for continuous variable systems, such as that described in Section 6, or one can convert the problem to Bell inequality tests on two qubits by mapping the two modes into two-qubit systems. In this and the following section, we will consider the latter case.

The Wigner function $W_{IPS}(\alpha, \beta)$ given in Eq. (54) is no longer positive definite and thus it can be used to test the violation of Bell's inequalities by means of homodyne detection, i.e., by measuring the quadratures x_ϑ and x_φ of the two IPS modes a and b, respectively, as proposed in [16, 17]. In this case, one can dichotomize the measured quadratures assuming as the outcome $+1$ when $x \geq 0$ and -1 otherwise. The nonlocality of $W_{IPS}(\alpha, \beta)$ in ideal conditions has been studied in [31], where we also discussed the effect of the homodyne detection efficiency η_H.

Let us now focus our attention on $W_{IPS}(\alpha, \beta)$ when the IPS process is applied to the TWB evolved through the noisy channel, namely, using substitutions (71). After the dichotomization of the homodyne outputs, one obtains the following Bell parameter:

$$\mathscr{B}_{HD} = E(\vartheta_1, \varphi_1) + E(\vartheta_1, \varphi_2) + E(\vartheta_2, \varphi_1) - E(\vartheta_2, \varphi_2), \tag{88}$$

where ϑ_k and φ_k are the phases of the two homodyne measurements at modes a and b, respectively, and

$$E(\vartheta_h, \varphi_k) = \int_{\mathbb{R}^2} dx_{\vartheta_h} dx_{\varphi_k} \, \text{sgn}[x_{\vartheta_h} x_{\varphi_k}] P(x_{\vartheta_h}, x_{\varphi_k}), \tag{89}$$

$P(x_{\vartheta_h}, x_{\varphi_k})$ being the joint probability of obtaining the two outcomes x_{ϑ_h} and x_{φ_k} [17]. As usual, violation of Bell's inequality is achieved when $|\mathscr{B}_{HD}| > 2$.

In Fig. 16, we plot $\mathscr{B}_{HD}$ for $\vartheta_1 = 0$, $\vartheta_2 = \pi/2$, $\varphi_1 = -\pi/4$, and $\varphi_2 = \pi/4$: as for the ideal case [17, 31], Bell's inequality is violated for a suitable choice of the squeezing parameter r. Obviously, the presence of noise reduces the violation, but we can see that the effect of thermal noise is not so large as in the case of the displaced parity test addressed in Section 6 (see Fig. 14). In Fig. 17, we plot $\mathscr{B}_{HD}$ as a function of T and ε: as for
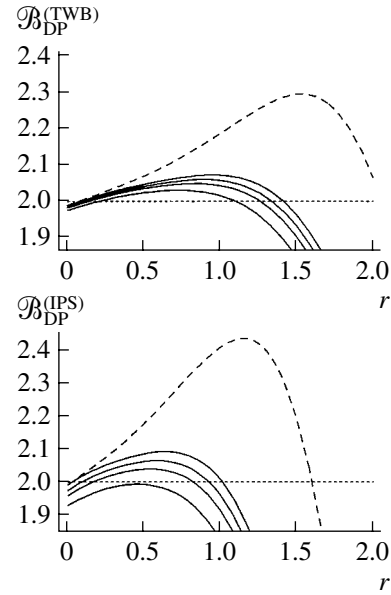

Fig. 14. Plots of the Bell parameters $\mathscr{B}_{DP}$ for the TWB (top) and IPS (bottom); we set $\mathscr{J} = 1.6 \times 10^{-3}$, which maximizes $\mathscr{B}_{DP}^{(TWB)}$, and put $T = 0.9999$ and $\varepsilon = 1$ for the IPS. The dashed lines refer to the absence of noise ($\Gamma t = N = 0$), whereas, for both plots, the solid lines are $\mathscr{B}_{DP}$ with $\Gamma t = 0.01$ and, from top to bottom, $N = 0$, 0.05, 0.1, and 0.2. In the ideal case, the maxima are $\mathscr{B}_{DP}^{(TWB)} = 2.32$ and $\mathscr{B}_{DP}^{(IPS)} = 2.43$, respectively.
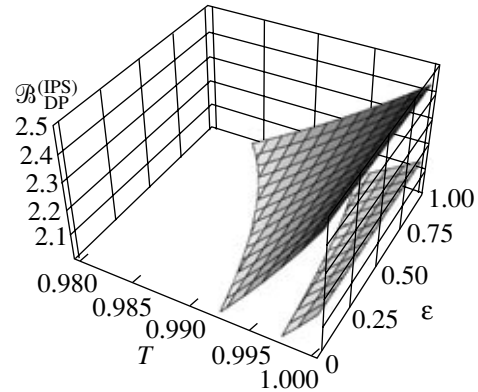

Fig. 15. The surfaces are plots of the Bell parameters $\mathscr{B}_{DP}$ for the IPS state as a function of T and ε for different values of Γt and $N = 0$: (top) $\Gamma t = 0$; (bottom) $\Gamma t = 0.005$. We set $\mathscr{J} = 1.6 \times 10^{-3}$ and $r = 1.16$. The value of the Bell parameter is mainly affected by T.

the displaced parity test (see Fig. 15), we can see that the main contribution to the Bell parameter is due to the transmissivity T.

Notice that the high efficiencies of this kind of detectors allow a loophole-free test of hidden variable theories [33], though the violations obtained are quite
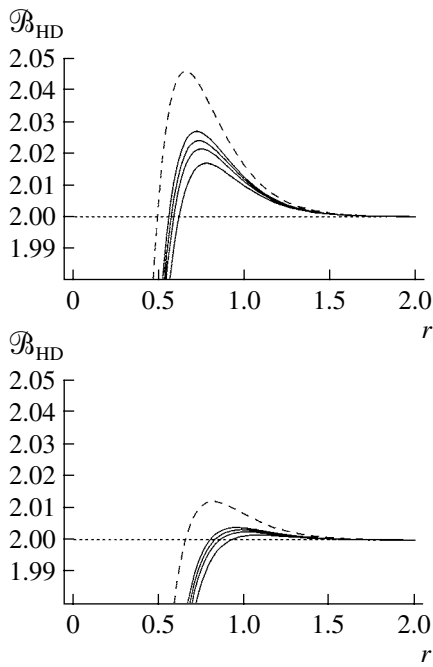
Fig. 16. Plots of the Bell parameter $\mathcal{B}_{HD}$ for the IPS states for two different values of the homodyne detection efficiency: $\eta_H = 1$ (top), and $\eta_H = 0.9$ (bottom). We set $\varepsilon = 1$ and $T = 0.99$. The dashed lines refer to the absence of noise ($\Gamma t = N = 0$), whereas, for both the plots, the solid lines are $\mathcal{B}_{HD}$ with $\Gamma t = 0.05$ and, from top to bottom, $N = 0, 0.05, 0.1$, and 0.2.
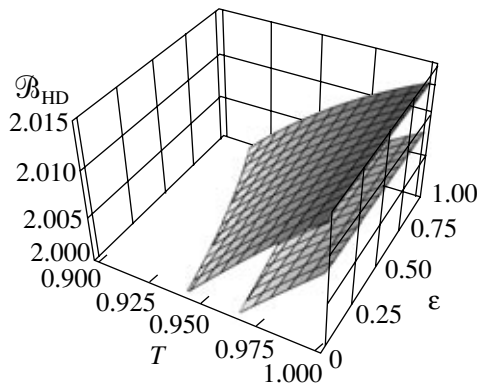

Fig. 17. The surfaces are plots of the Bell parameters $\mathcal{B}_{HD}$ for the IPS state as a function of T and ε for $N = 0$ and different values of (top) $\Gamma t = 0$, and (bottom) $\Gamma t = 0.025$. We set $r = 0.82$ and $\eta_H = 0.9$.

small. This is due to the intrinsic information loss of the binning process, which is used to convert the continuous homodyne data in dichotomic results [34].

8. NONLOCALITY AND PSEUDOSPIN TEST

Another way to map two-mode continuous variable system into a two-qubit system is by means of the pseu-

dospin test: this consists in measuring three single-mode Hermitian operators S_k satisfying the Pauli matrix algebra $[S_h, S_k] = 2i\varepsilon_{hkl}S_l$, $S_k^2 = \mathbb{I}$, $h, k, l = 1, 2, 3$, and ε_{hkl} is the totally antisymmetric tensor with $\varepsilon_{123} = +1$ [35, 36]. For the sake of clarity, we will refer to S_1, S_2, and S_3 as S_x, S_y, and S_z, respectively. In this way, one can write the following correlation function:

$$E(\mathbf{a}, \mathbf{b}) = \langle (\mathbf{a} \cdot \mathbf{S})(\mathbf{b} \cdot \mathbf{S}) \rangle, \tag{90}$$

where $\mathbf{a}$ and $\mathbf{b}$ are unit vectors such that

$$\mathbf{a} \cdot \mathbf{S} = \cos\vartheta_a S_z + \sin\vartheta_a(e^{i\varphi_a}S_- + e^{-i\varphi_a}S_+), \tag{91}$$

$$\mathbf{b} \cdot \mathbf{S} = \cos\vartheta_b S_z + \sin\vartheta_b(e^{i\varphi_b}S_- + e^{-i\varphi_b}S_+), \tag{92}$$

with $S_\pm = \frac{1}{2}(S_x \pm iS_y)$. In the following, without loss of generality, we set $\varphi_k = 0$. Finally, the Bell parameter reads

$$\begin{aligned} \mathcal{B}_{PS} &= E(\mathbf{a}_1, \mathbf{b}_1) + E(\mathbf{a}_1, \mathbf{b}_2) \\ &+ E(\mathbf{a}_2, \mathbf{b}_1) - E(\mathbf{a}_2, \mathbf{b}_2), \end{aligned} \tag{93}$$

corresponding to the CHSH Bell's inequality $|\mathcal{B}_{PS}| \le 2$. In order to study Eq. (93), we should choose a specific representation of the pseudospin operators; note that, as pointed out in [37, 38], the violation of Bell's inequalities for continuous variable systems depends, in addition to the orientational parameters, on the chosen representation, since different S_k leads to different expectation values of $\mathcal{B}_{PS}$. Here we consider the pseudospin operators corresponding to the Wigner functions [37]

$$W_x(\alpha) = \frac{1}{\pi}\text{sgn}[\Re e[\alpha]], \quad W_z(\alpha) = -\frac{1}{2}\delta^{(2)}(\alpha), \tag{94}$$

$$W_y(\alpha) = -\frac{1}{2\pi}\delta(\Re e[\alpha])\mathcal{P}\frac{1}{\Im m[\alpha]}, \tag{95}$$

where $\mathcal{P}$ denotes the Cauchy principal value. Using (94), one obtains

$$\begin{aligned} E_{TWB}(\mathbf{a}, \mathbf{b}) &= \cos\vartheta_a\cos\vartheta_b \\ &+ \frac{2\sin\vartheta_a\sin\vartheta_b}{\pi}\arctan[\sinh(2r)] \end{aligned} \tag{96}$$

for the TWB and

$$\begin{aligned} E_{IPS}(\mathbf{a}, \mathbf{b}) &= \sum_{k=1}^{4}\frac{\mathscr{C}_k}{p_{11}(r, T, \varepsilon)}\left[\frac{\cos\vartheta_a\cos\vartheta_b}{4}\right. \\ &\left.+ \frac{2\sin\vartheta_a\sin\vartheta_b}{\pi\mathscr{A}_k}\arctan\left(\frac{2B_0T + h_k}{\sqrt{\mathscr{A}_k}}\right)\right] \end{aligned} \tag{97}$$

for the IPS, where $\mathscr{A}_k = (b - f_k)(b - g_k) - (2B_0T + h_k)^2$, and all the other quantities have been denned in Section 3.
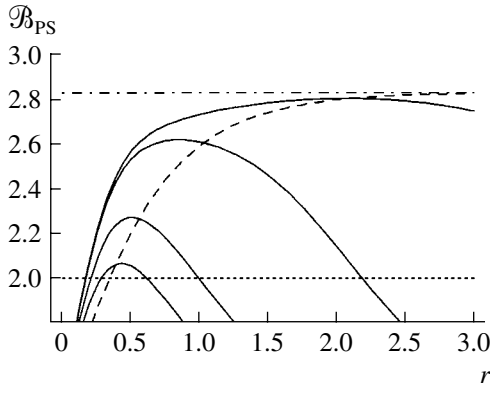
Fig. 18. Plots of the Bell parameter $\mathcal{B}_{PS}$, in the ideal case ($\Gamma t = N = 0$): the dashed line refers to the TWB, whereas the solid lines refer to the IPS with $\varepsilon = 1$ and, from top to bottom, $T = 0.9999$, 0.99, 0.9, and 0.8. There is a threshold value for r below which IPS gives a higher violation than TWB. Note that there is also a region of small values of r for which the IPS state violates Bell's inequality while the TWB does not. The dot–dashed line is the maximal violation value $2\sqrt{2}$.

In Fig. 18, we plot $\mathcal{B}_{PS}$ for the TWB and IPS in the ideal case, namely, in the absence of dissipation and thermal noise. For all the figures, we set $\vartheta_{a_1} = 0$, $\vartheta_{a_2} = \pi/2$, and $\vartheta_{b_1} = -\vartheta_{b_2} = \pi/4$. As usual, the IPS leads to better results for small values of r, whereas $\mathcal{B}_{PS}^{(TWB)} \longrightarrow 2\sqrt{2}$ as $r \longrightarrow \infty$, $\mathcal{B}_{PS}^{(IPS)}$ has a maximum and then falls below the threshold 2 as r increases. It is interesting to note that there is a region of small values of r for which $\mathcal{B}_{PS}^{(TWB)} \leq 2 < \mathcal{B}_{PS}^{(IPS)}$; i.e., the IPS process can increase the nonlocal properties of a TWB which does not violates Bell's inequality for the pseudospin test in such a way that the resulting state violates it. This
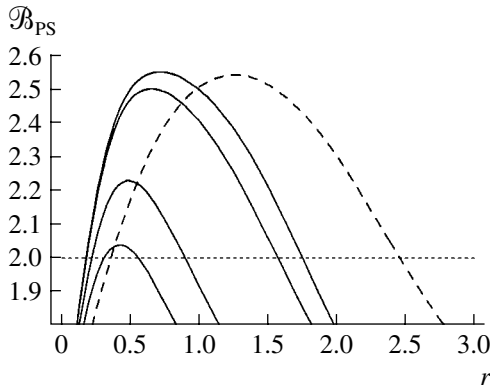
fact is also present in the case of the displaced parity test described in Section 6, but by using the pseudospin test the effect is enhanced. Notice that the maximum violations for the IPS occur for a range of values r which are experimentally achievable.

In Fig. 19, we consider the presence of the dissipation alone and vary T. We can see that IPS is effective also when the effective transmissivity T is not very high. We take into account the effect of dissipation and thermal noise in Figs. 20 and 21: we can conclude that IPS is quite robust with respect to this source of noise and, moreover, one can think of employing IPS as a useful resource in order to reduce the effect of noise. In Fig. 22, we plot $\mathcal{B}_{PS}^{(IPS)}$ as a function of T and ε: the main effect on the Bell parameter is due to the transmissivity T, as in the previous cases.

9. NONLOCALITY AND ON/OFF PHOTODETECTION

The nonlocality test we are going to analyze is schematically depicted in Fig. 23. Two modes of the de-Gaussified TWB radiation field, a and b, described by the density matrix ϱ, are locally displaced by an amount α and β, respectively, and are finally revealed by on/off photodetectors, i.e., detectors which have no output when no photon is detected and a fixed output when one or more photons are detected. The action of an on/off detector is described by the following two-value positive operator-valued measure (POVM) $\{\Pi_{0,\eta,D}, \Pi_{1,\eta,D}\}$ [2]:

$$\Pi_{0,\eta,D} = \frac{1}{1+D} \sum_{k=0}^{\infty} \left(1 - \frac{\eta}{1+D}\right)^k |k\rangle\langle k|, \qquad (98a)$$

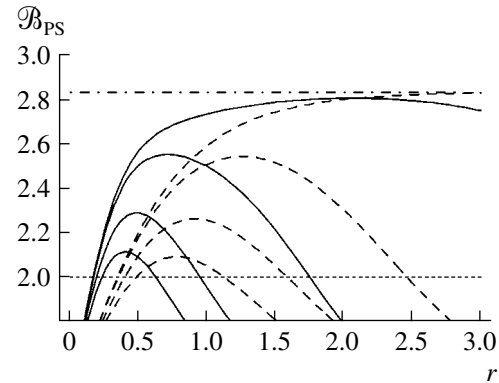$$\Pi_{1,\eta,D} = \mathbb{1} - \Pi_{0,\eta,D}, \qquad (98b)$$

Fig. 19. Plots of the Bell parameter $\mathcal{B}_{PS}$ for $\Gamma t = 0.01$: the dashed line refers to the TWB, whereas the solid lines refer to the IPS with $\varepsilon = 1$ and, from top to bottom, $T = 0.9999$, 0.99, 0.9, and 0.8. The same comments as in Fig. 18 still hold.

Fig. 20. Plots of the Bell parameter $\mathcal{B}_{PS}$ for different values of Γt and in the absence of thermal noise ($N = 0$): the dashed lines refer to the TWB, whereas the solid ones refer to the IPS with $T = 0.9999$ and $\varepsilon = 1$; for both the TWB and IPS we set, from top to bottom, $\Gamma t = 0$, 0.01, 0.05, and 0.1. The dot–dashed line is the maximal violation value $2\sqrt{2}$.
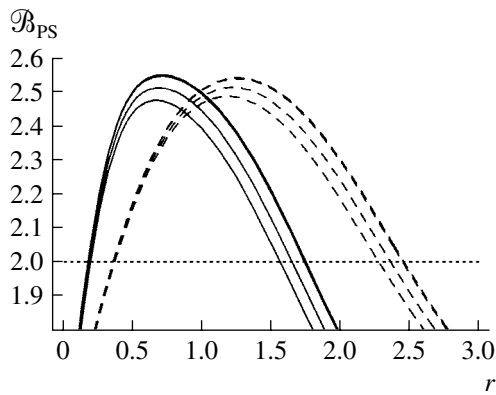
Fig. 21. Plots of the Bell parameter $\mathcal{B}_{PS}$ for $\Gamma t = 0.01$ and different values $N = 0$: the dashed lines refer to the TWB, whereas the solid ones refer to the IPS with $T = 0.9999$ and $\varepsilon = 1$; for both the TWB and IPS we set, from top to bottom, $N = 0, 0.01, 0.1,$ and 0.2.

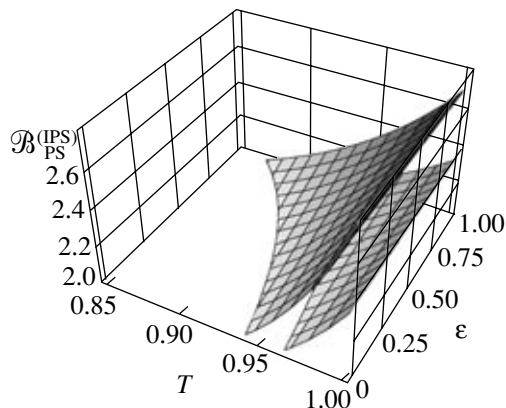**Fig. 22.** The surfaces are plots of the Bell parameters $\mathcal{B}_{PS}^{(IPS)}$ for the IPS state as a function of T and ε for $N = 0$ and different values of Γt: (top) $\Gamma t = 0$ and (bottom) $\Gamma t = 0.025$. We set $r = 0.86$.
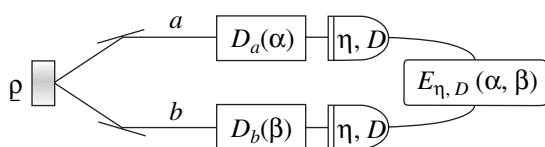

Fig. 23. Scheme of the nonlocality test based on displaced on/off photodetection: the two modes a and b of a bipartite state ϱ are locally displaced by an amount of α and β, respectively, and then revealed through on/off photodetection. The corresponding correlation function violates Bell's inequalities for dichotomic measurements for a suitable choice of the parameters α and β, depending on the kind of state under investigation. The violation also holds for non-unit quantum efficiency and nonzero dark counts.

where η is the quantum efficiency and D is the mean number of dark counts, i.e., of clicks with vacuum input. In writing Eq. (98), we have considered the thermal background as the origin of dark counts. An analogous expression may be written for a Poissonian background [19]. For small values of the mean number D of dark counts (as generally happens at optical frequencies), the two kinds of background are indistinguishable.

Overall, taking into account the displacement, the measurement on both modes a and b is described by the POVM (we are assuming the same quantum efficiency and dark counts for both the photodetectors)

$$\Pi_{hk}^{(\eta, D)}(\alpha, \beta) = \Pi_h^{(h, D)}(\alpha) \otimes \Pi_k^{(\eta, D)}(\beta), \qquad (99)$$

where h, $k = 0$, 1 and $\Pi_h^{(\eta, D)}(z) \equiv D(z)\Pi_{h, \eta, D}D^\dagger(z)$, $D(z) = \exp\{za^\dagger - z^*a\}$ is the displacement operator and $z \in \mathbb{C}$ is a complex parameter.

In order to analyze the nonlocality of the state ϱ, we introduce the following correlation function:

$$E_{\eta, D}(\alpha, \beta) = \sum_{h, k = 0}^{1} (-)^{h+k}\langle\Pi_{hk}^{(\eta, D)}(\alpha, \beta)\rangle \qquad (100)$$
$$= 1 + 4\mathcal{I}_{\eta, D}(\alpha, \beta) - 2[\mathcal{G}_{\eta, D}(\alpha) + \mathcal{Y}_{\eta, D}(\beta)],$$

where

$$\mathcal{I}_{\eta, D}(\alpha, \beta) = \langle\Pi_{00}^{(\eta, D)}(\alpha, \beta)\rangle, \qquad (101)$$

$$\mathcal{G}_{\eta, D}(\alpha) = \langle\Pi_0^{(\eta, D)}(\alpha) \otimes \mathbb{I}\rangle, \qquad (102)$$

$$\mathcal{Y}_{\eta, D}(\beta) = \langle\mathbb{I} \otimes \Pi_0^{(\eta, D)}(\beta)\rangle, \qquad (103)$$

and $\langle A\rangle \equiv \text{Tr}[\varrho A]$ denotes the ensemble average on both the modes. The so-called Bell parameter is defined by considering four different values of the complex displacement parameters as follows:

$$\mathcal{B}_{\eta, D} = E_{\eta, D}(\alpha, \beta) + E_{\eta, D}(\alpha', \beta)$$
$$+ E_{\eta, D}(\alpha, \beta') - E_{\eta, D}(\alpha', \beta') \qquad (104)$$

$$= 2 + 4\{\mathcal{I}_{\eta, D}(\alpha, \beta) + \mathcal{I}_{\eta, D}(\alpha', \beta) + \mathcal{I}_{\eta, D}(\alpha, \beta')$$
$$- \mathcal{I}_{\eta, D}(\alpha', \beta') - \mathcal{G}_{\eta, D}(\alpha) - \mathcal{Y}_{\eta, D}(\beta)\}. \qquad (105)$$

Any local theory implies that $|\mathcal{B}_{\eta, D}|$ satisfies the CHSH version of the Bell inequality, i.e., $|\mathcal{B}_{\eta, D}| \leq 2 \; \forall\alpha, \alpha', \beta,$ β' [29], while a quantum mechanical description of the same kind of experiments does not impose this bound.

Notice that, using Eqs. (98) and (101)–(103), we obtain the following scaling properties for the functions $\mathcal{I}_{\eta, D}(\alpha, \beta)$, $\mathcal{G}_{\eta, D}(\alpha)$, and $\mathcal{Y}_{\eta, D}(\beta)$:

$$\mathcal{I}_{\eta, D}(\alpha, \beta) = \left(\frac{1}{1 + D}\right)^2 \mathcal{I}_{\eta/(1+D)}(\alpha, \beta), \qquad (106)$$

$$\mathscr{G}_{\eta, D}(\alpha) = \frac{1}{1 + D}\mathscr{G}_{\eta/(1 + D)}(\alpha), \qquad (107)$$

$$\mathscr{Y}_{\eta, D}(\beta) = \frac{1}{1 + D}\mathscr{Y}_{\eta/(1 + D)}(\beta), \qquad (108)$$

where $\mathscr{I}_{\eta} = \mathscr{I}_{\eta, 0}$, $\mathscr{G}_{\eta} = \mathscr{G}_{\eta, 0}$, and $\mathscr{Y}_{\eta} = \mathscr{Y}_{\eta, 0}$. Therefore, it will be enough to study the Bell parameter for $D = 0$, namely, $\mathscr{B}_{\eta} = \mathscr{B}_{\eta, 0}$, and then we can use Eqs. (106)–(108) to take into account the effects of nonnegligible dark counts. From now on, we will assume $D = 0$ and suppress the explicit dependence on D. Notice that, using expression (105) for the Bell parameter, we can rewrite the CHSH inequality $|\mathscr{B}_{\eta, D}| \leq 2$ as

$$-1 < \mathscr{I}_{\eta, D}(\alpha, \beta) + \mathscr{I}_{\eta, D}(\alpha', \beta) + \mathscr{I}_{\eta, D}(\alpha, \beta')$$
$$- \mathscr{I}_{\eta, D}(\alpha', \beta') - \mathscr{G}_{\eta, D}(\alpha) - \mathscr{Y}_{\eta, D}(\beta) < 0, \qquad (109)$$

which represents the CH version of the Bell inequality for our system [39].

In order to simplify the calculations, throughout this section we will use the Wigner formalism. The Wigner functions associated with the elements of the POVM (98) for $D = 0$ are given by [19]

$$W[\Pi_{0, \eta}](z) = \frac{\Delta_{\eta}}{\pi\eta}\exp\{-\Delta_{\eta}|z|^2\}, \qquad (110)$$

$$W[\Pi_{1, \eta}](z) = W[\mathbb{1}](z) - W[\Pi_{0, \eta}](z), \qquad (111)$$

with $\Delta_{\eta} = 2\eta/(2 - \eta)$ and $W[\mathbb{1}](z) = \pi^{-1}$. Then, noticing that for any operator O one has

$$W[D(\alpha)OD^{\dagger}(\alpha)](z) = W[O](z - \alpha), \qquad (112)$$

one can get $W[D(\alpha)\Pi_{0, \eta}D^{\dagger}(\alpha)](z)$ given by

$$W[D(\alpha)\Pi_{0, \eta}D^{\dagger}(\alpha)](z) = W[\Pi_{0, \eta}](z - \alpha), \quad (113)$$

and therefore

$$W[\Pi_{00}^{(\eta, 0)}(\alpha, \beta)](z, w)$$
$$= W[\Pi_{0, \eta}](z - \alpha)W[\Pi_{0, \eta}](w - \beta), \qquad (114)$$

$$W[\Pi_{0, \eta}(\alpha) \otimes \mathbb{1}](z, w) = W[\Pi_{0, \eta}](z - \alpha)\pi^{-1}, \quad (115)$$

$$W[\mathbb{1} \otimes \Pi_{0, \eta}(\beta)](z, w) = \pi^{-1}W[\Pi_{0, \eta}](w - \beta). \quad (116)$$

Finally, thanks to the trace rule expressed in the phase space of two modes, i.e.,

$$\text{Tr}[O_1O_2]$$
$$= \pi^2\int_{\mathbb{C}^2}d^2z\,d^2w\,W[O_1](z, w)W[O_2](z, w), \qquad (117)$$

one can evaluate the functions $\mathscr{I}_{\eta}(\alpha, \beta)$, $\mathscr{G}_{\eta}(\alpha)$, and $\mathscr{Y}_{\eta}(\beta)$, and in turn the Bell parameter $\mathscr{B}_{\eta}$ in Eq. (105), as a sum of Gaussian integrals in the complex plane.
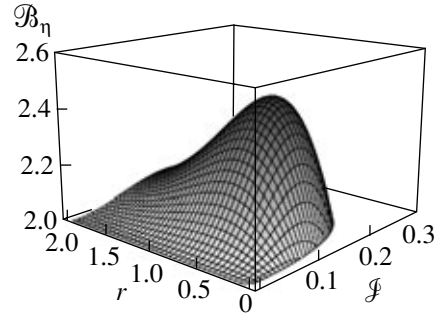
Fig. 24. Plot of $\mathscr{B}_{\eta}$ for a TWB as a function of $\mathscr{J}$ and the TWB squeezing parameter r in the case of ideal (i.e., $\eta = 1$) on/off photodetection. The maximum violation is $\mathscr{B}_{\eta} = 2.45$, which is obtained when $\mathscr{J} = 0.16$ and $r = 0.74$.

Let us now consider the TWB (25). Since the Wigner functions of the TWB and of the POVM (99) are Gaussian, it is quite simple to evaluate $\mathscr{I}_{\eta}(\alpha, \beta)$, $\mathscr{G}_{\eta}(\alpha)$, and $\mathscr{Y}_{\eta}(\beta)$ of correlation function (100) and then $\mathscr{B}_{\eta}$; we have

$$\mathscr{I}_{\eta}(\alpha, \beta) = \frac{\mathcal{M}_{\eta}(r)}{\eta^2\sqrt{\text{Det}[\boldsymbol{\sigma}_0]}} \qquad (118)$$
$$\times \exp\{-\tilde{F}_{\eta}(|\alpha|^2 + |\beta|^2) + \tilde{H}_{\eta}(\alpha\beta + \alpha*\beta*)\},$$

$$\mathscr{G}_{\eta}(\alpha) = \mathscr{Y}_{\eta}(\alpha) = \frac{(2\sqrt{\text{Det}[\boldsymbol{\sigma}_0]})^{-1}\Delta_{\eta}}{[2(\tilde{A}_0^2 - \tilde{B}_0^2) + \tilde{A}_0\Delta_{\eta}]}$$
$$\times \exp\left\{-\frac{2\Delta_{\eta}}{2(\tilde{A}_0^2 - \tilde{B}_0^2) + \tilde{A}_0\Delta_{\eta}}|\alpha|^2\right\}, \qquad (119)$$

with

$$\tilde{F}_{\eta} \equiv \tilde{F}_{\eta}(r) = \Delta_{\eta} - (2\tilde{A}_0 + \Delta_{\eta})\mathcal{M}_{\eta}(r), \qquad (120)$$

$$\tilde{H}_{\eta} \equiv \tilde{H}_{\eta}(r) = 2\tilde{B}_0\mathcal{M}_{\eta}(r), \qquad (121)$$

$$\mathcal{M}_{\eta}(r) = \frac{\Delta_{\eta}^2}{4(\tilde{A}_0^2 - \tilde{B}_0^2) + 4\tilde{A}_0\Delta_{\eta} + \Delta_{\eta}^2}. \qquad (122)$$

In order to study Eq. (105), we consider the parametrization $\alpha = -\beta = \mathscr{J}$ and $\alpha' = -\beta' = -\sqrt{11}\,\mathscr{J}$ (more details are given in [19]). The parametrization was chosen after a semi-analytical analysis and maximizes the violation of Bell's inequality (for $\eta = 1$). In Fig. 24, we plot $\mathscr{B}_{\eta}$ for $\eta = 1$: as one can see that the inequality $|\mathscr{B}_{\eta}| \leq 2$ is violated for a wide range of parameters and that the maximum violation ($\mathscr{B}_{\eta} = 2.45$) is achieved when $\mathscr{J} = 0.16$ and $r = 0.74$. The effect of nonunit efficiency in the detection stage is to reduce the violation; this is shown in Fig. 25, where we plot $\mathscr{B}_{\eta}$ as a function of $\mathscr{J}$ with $r = 0.74$ for different values of the quantum efficiency. Note that, although the violation in the ideal case, i.e.,
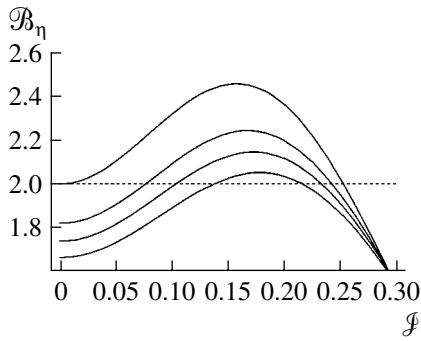
Fig. 25. Plot of $\mathcal{B}_\eta$ for a TWB as a function of $\mathcal{J}$ with $r = 0.74$ for different values of η: from top to bottom, $\eta = 1.0$, 0.9, 0.85, and 0.80.
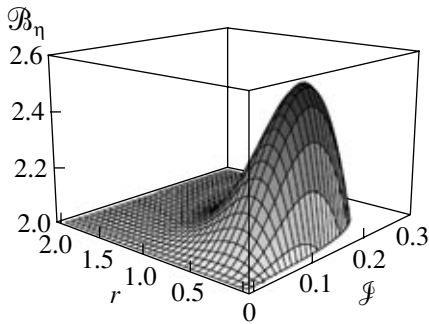

Fig. 26. Plot of $\mathcal{B}_\eta$ for the IPS state with $T = 0.9999$ and $\varepsilon = 1$ as a function of $\mathcal{J}$ and the TWB squeezing parameter r in the case of ideal (i.e., $\eta = 1$) on/off photodetection. The maximum violation is $\mathcal{B}_\eta = 2.53$, which is obtained when $\mathcal{J} = 0.16$ and $r = 0.39$.
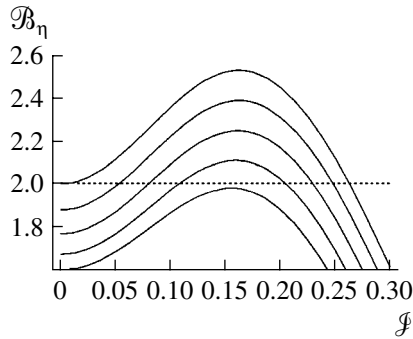

Fig. 27. Plot of 5 $\mathcal{B}_\eta$ for the IPS state as a function of $\mathcal{J}$ with $r = 0.39$ for different values of T and $\varepsilon = 1$ in the ideal case (i.e., $\eta = 1$): from top to bottom, $T = 0.9999$, 0.9, 0.8, 0.7, and 0.6.

$\eta = 1$, is smaller than for the Bell states, the TWBs are more robust when one takes into account nonunit quantum efficiency.

In the case of state (54), correlation function (100) reads (for the sake of simplicity, we do not write explicitly the dependence on r, T, and ε)

$$E_\eta(\alpha, \beta) = 1 + \frac{1}{p_{11}(r, T, \varepsilon)} \sum_{k=1}^{4} \mathcal{C}_k \{ 4 \mathcal{I}_\eta^{(k)}(\alpha, \beta) \tag{123}$$
$$- 2[\mathcal{G}_\eta^{(k)}(\alpha) + \mathcal{Y}_\eta^{(k)}(\beta)] \},$$

where

$$\mathcal{I}_\eta^{(k)}(\alpha, \beta) = \frac{\mathcal{M}_\eta^{(k)}(r, T, \varepsilon)}{\eta^2} \tag{124}$$
$$\times \exp\{-\tilde{G}_\eta^{(k)}|\alpha|^2 - \tilde{F}_\eta^{(k)}|\beta|^2 + \tilde{H}_\eta^{(k)}(\alpha\beta + \alpha^*\beta^*)\},$$

$$\mathcal{G}_\eta^{(k)}(\alpha) = \frac{\Delta_\eta}{[G_k(F_k + \Delta_\eta) - H_k^2]\eta} \tag{125}$$
$$\times \exp\left\{ -\frac{(F_k G_k - H_k^2)\Delta_\eta}{G_k(F_k + \Delta_\eta) - H_k^2}|\alpha|^2 \right\},$$

$$\mathcal{Y}_\eta^{(k)}(\beta) = \frac{\Delta_\eta}{[F_k(G_k + \Delta_\eta) - H_k^2]\eta} \tag{126}$$
$$\times \exp\left\{ -\frac{(F_k G_k - H_k^2)\Delta_\eta}{F_k(G_k + \Delta_\eta) - H_k^2}|\beta|^2 \right\},$$

with $\tilde{F}_\eta^{(k)} \equiv \tilde{F}_\eta^{(k)}(r, T, \varepsilon)$, $\tilde{G}_\eta^{(k)} \equiv \tilde{G}_\eta^{(k)}(r, T, \varepsilon)$, and $\tilde{H}_\eta^{(k)} \equiv \tilde{H}_\eta^{(k)}(r, T, \varepsilon)$ given by

$$\tilde{F}_\eta^{(k)} = \Delta_\eta - (F_k + \Delta_\eta)\mathcal{M}_\eta^{(k)}(r, T, \varepsilon), \tag{127}$$

$$\tilde{G}_\eta^{(k)} = \Delta_\eta - (G_k + \Delta_\eta)\mathcal{M}_\eta^{(k)}(r, T, \varepsilon), \tag{128}$$

$$\tilde{H}_\eta^{(k)} = H_k \mathcal{M}_\eta^{(k)}(r, T, \varepsilon), \tag{129}$$

$$\mathcal{M}_\eta^{(k)}(r, T, \varepsilon) = \frac{\Delta_\eta^2}{(F_k + \Delta_\eta)(G_k + \Delta_\eta) - H_k^2}, \tag{130}$$

where $F_k = b - f_h$, $G_k = b - g_h$, and $H_k = 2\tilde{B}_0 T - h_k$, and all the involved quantities are the same as in Eq. (54).

In order to study Eq. (105), we consider the parametrization $\alpha = -\beta = \mathcal{J}$ and $\alpha' = -\beta' = -\sqrt{11}\mathcal{J}$. This parametrization was chosen after a semi-analytical analysis and maximizes the violation of Bell's inequality (for $\eta = 1$) [19]. The results are showed in Figs. 26 and 27 for $\eta = 1$ and $\varepsilon = 1$: we can see that the IPS enhances the violation of the inequality $|\mathcal{B}_\eta| \leq 2$ for small values of r (see also [10, 15, 31]). Moreover, as one may expect, the maximum of violation is achieved
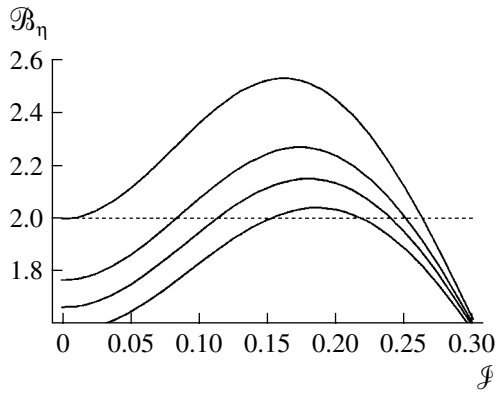
Fig. 28. Plot of $\mathcal{B}_\eta$ for the IPS state as a function of $\mathcal{J}$ with $r = 0.39$, $T = 0.9999$, $\varepsilon = 1$, and for different values of η: from top to bottom, $\eta = 1.0, 0.9, 0.85$, and 0.8.
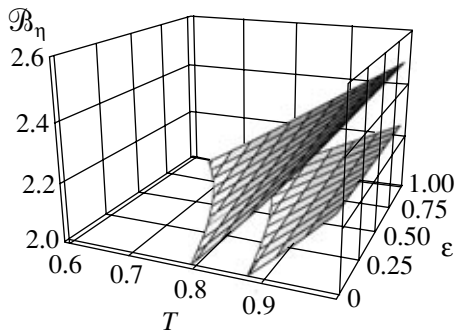

Fig. 29. Plot of $\mathcal{B}_\eta$ for the IPS state as a function T and ε with $\mathcal{J} = 0.16$, $r = 0.39$, and, from top to bottom, $\eta = 0.99$ and 0.90. The main effect on $\mathcal{B}_\eta$ is due to the transmissivity T.
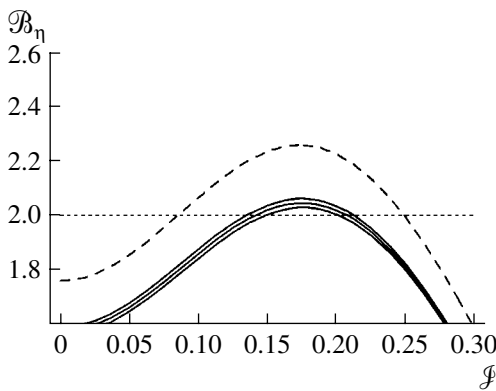

Fig. 30. Plot of $\mathcal{B}_\eta$ for the IPS state as a function of $\mathcal{J}$ with $r = 0.39$, $T = 0.99$, $\varepsilon = 1$, $\eta = 0.9$, and $\Gamma t = 0.1$ for different values of N: from top to bottom (solid lines), $N = 0, 0.01$, and 0.02. The dashed line is $\mathcal{B}_\eta$ with $\Gamma t = N = 0$.

as $T \longrightarrow 1$, whereas, decreasing the effective transmission of the IPS process, one finds that the inequality becomes satisfied for all values of r, as we can see in Fig. 27 for $T = 0.6$.

In Fig. 28, we plot $\mathcal{B}_\eta$ for the IPS with $T = 0.9999$, $\varepsilon = 1$, and different η. As for the TWB, we can also have violation of Bell's inequality for detection efficiencies near 80%. As for the Bell states and the TWB, a η- and r-dependent choice of the parameters in Eq. (105) can improve this result. The effect on a nonunit ε is studied in Fig. 29, where we plot $\mathcal{B}_\eta$ as a function of T and ε and fixed values of the other involved parameters. We can see that the main effect on the Bell parameter is due to the transmissivity T.

Finally, the effect of dissipation and thermal noise affecting the propagation of the TWB before the IPS process is shown in Fig. 30.

10. CONCLUSIONS

We have analyzed in detail a photon-subtraction scheme to de-Gaussify states of radiation and, in particular, to enhance nonlocal properties of twin-beams. The scheme is based on conditional inconclusive subtraction of photons (IPS), which may be achieved by means of linear optical components and avalanche on/off photodetectors. The IPS process can be implemented with current technology and, indeed, application to a single-mode state has been recently realized with high conditional probability [11].

We found that the IPS process improves the fidelity of coherent state teleportation and showed, by using several different nonlocality tests, that it also enhances nonlocal correlations. IPS may be profitably used also on nonmaximally mixed entangled states, such as the ones coming from the evolution of TWB in a noisy channel. In addition, the effectiveness of the process is not dramatically influenced either by the transmissivity of the beam splitter used to subtract photons or by the quantum efficiency of the detectors used to reveal them.

We conclude that IPS on TWB is a robust and realistic scheme to improve quantum information processing with CV radiation states.

ACKNOWLEDGMENTS

REFERENCES

1. S. Braunstein and P. van Loock, Rev. Mod. Phys. **77**, 513 (2005).
2. A. Ferraro, S. Olivares, and M. G. A. Paris, "Gaussian States in Quantum Information", *Napoli Series on Physics and Astrophysics* (Bibliopolis, Napoli, 2005); quant-ph/0503237.
3. *Quantum Interferometry III*, Ed. by F. De Martini, G. Denardo, and L. Hardy, Special issue of Fort. Phys. **48** (2000); *Quantum Interferometry IV*, Special issue of Fort. Phys. **51** (2003).
4. *Quantum Communication, Computing and Measurement II*, Ed. by P. Kumar, G. M. D'Ariano, and O. Hirota,

(Kluwer, Dordrecht, 2000); *Quantum Communication, Computing and Measurement III,* Ed. by P. Tombesi and O. Hirota (Kluwer, Dordrecht, 2001).

5. A. Furusawa et al., Science **282**, 706 (1998); S. L. Braunstein and H. J. Kimble, Phys. Rev. Lett. **80**, 869 (1998).

6. S. L. Braunstein and H. J. Kimble, Phys. Rev. A **61**, 042302 (2000); J. Jing et al., Phys. Rev. Lett. **90**, 167903 (2003).

7. H. Yonezawa, T. Aoki, and A. Furusawa, Nature **431**, 430 (2004).

8. T. Opatrný, G. Kurizki, and D.-G. Welsch, Phys. Rev. A **61**, 032302 (2000).

9. P. T. Cochrane, T. C. Ralph, and G. J. Milburn, Phys. Rev. A **65**, 062306 (2002).

10. S. Olivares, M. G. A. Paris, and R. Bonifacio, Phys. Rev. A **67**, 032314 (2003).

11. J. Wenger, R. Tualle-Brouri, and P. Grangier, Phys. Rev. Lett. **92**, 153601 (2004).

12. M. S. Kim, E. Park, P. L. Knight, and H. Jeong, Phys. Rev. A **71**, 013801 (2005).

13. S. Olivares and M. G. A. Paris, J. Opt. B: Quantum Semiclass. Opt. **7**, S616 (2005).

14. S. Olivares and M. G. A. Paris, Phys. Rev. A **70**, 032112 (2004).

15. S. Olivares and M. G. A. Paris, J. Opt. B: Quantum and Semiclass. Opt. **7**, S392 (2005).

16. H. Nha and H. J. Carmichael, Phys. Rev. Lett. **93**, 020401 (2004).

17. R. García-Patrón, et al., Phys. Rev. Lett. **93**, 130409 (2004); R. García-Patrón, J. Fiurášek, and N. J Cerf, Phys. Rev. A **71**, 022105 (2005).

18. S. Daffer and P. L. Knight, Phys. Rev. A **72**, 032509 (2005).

19. C. Invernizzi, S. Olivares, M. G. A. Paris, and K. Banszek, Phys. Rev. A **72**, 042105 (2005).

20. M. Dakna et al, Phys. Rev. A **55**, 3184 (1997).

21. F. Zappa, A. L. Lacaita, S. D. Cova, and P. Lovati, Opt. Eng. **35**, 938 (1996); D. Achilles, C. Silberhorn, S. Sliwa, et al., Opt. Lett. **28**, 2387 (2003).

22. G. Di Giuseppe, A. V. Sergienko, B. E. A. Saleh, and M. C. Teich in *Quantum Information and Computation*, Ed. by E. Donkor, A. R. Pirich, and H. E. Brandt, Proc. SPIE **5105**, 39 (2003).

23. A. R. Rossi, S. Olivares, and M. G. A. Paris, Phys. Rev. A **70**, 055801 (2004).

24. M. Bondani et. al., Phys. Rev. Lett. **95**, 063602 (2005).

25. D. Walls and G. Milburn, *Quantum Optics* (Springer, Berlin, 1994).

26. S. Olivares and M. G. A. Paris, J. Opt. B: Quantum Semiclass. Opt. **6**, 69 (2004).

27. A. Serafini, F. Illuminati, M. G. A. Paris, and S. De Siena, Phys. Rev. A **69**, 023318 (2004).

28. M. G. A. Paris, M. Cola, and R. Bonifacio, Phys. Rev. A **67**, 042104 (2003).

29. J. F. Clauser, M. A. Home, A. Shimony, and R. A. Holt, Phys. Rev. Lett. **23**, 880 (1969).

30. K. Banaszek and K. Wódkiewicz, Phys. Rev. A **58**, 4345 (1998).

31. S. Olivares and M. G. A. Paris, Phys. Rev. A **70**, 032112 (2004).

32. H. Jeong et al., Phys. Rev. A **67**, 012106 (2003).

33. A. Gilchrist, P. Deuar, and M. D. Reid, Phys. Rev. Lett. **80**, 3169 (1998); A. Gilchrist, P. Deuar, and M. D. Reid, Phys. Rev. A **60**, 4259(1999).

34. W. J. Munro, Phys. Rev. A **59**, 4197 (1999).

35. R. Filip and L. Mista, Phys. Rev. A **66**, 044309 (2002).

36. Z.-B. Chen, J.-W. Pan, G. Hou, and Y.-D. Zhang, Phys. Rev. Lett. **88**, 040406 (2002).

37. G. Gour et al., Phys. Lett. A **324**, 415 (2003); M. Revzen et al., Phys. Rev. A **71**, 022103 (2005).

38. A. Ferraro and M. G. A. Paris, J. Opt. B: Quantum Semiclass. Opt. **7**, 174 (2005).

39. J. F. Clauser and M. A. Horne, Phys, Rev. D **10**, 526 (1974).